isvr Institute of Sound and Vibration Research

Sources of Error and Confidence Intervals for SEA Parameters of Two Coupled Rectangular Plates

W.S. Park, D.J. Thompson and N.S. Ferguson

ISVR Technical Memorandum 856

December 2000

University of Southampton

SCIENTIFIC PUBLICATIONS BY THE ISVR

Technical Reports are published to promote timely dissemination of research results by ISVR personnel. This medium permits more detailed presentation than is usually acceptable for scientific journals. Responsibility for both the content and any opinions expressed rests entirely with the author(s).

Technical Memoranda are produced to enable the early or preliminary release of information by ISVR personnel where such release is deemed to the appropriate. Information contained in these memoranda may be incomplete, or form part of a continuing programme; this should be borne in mind when using or quoting from these documents.

Contract Reports are produced to record the results of scientific work carried out for sponsors, under contract. The ISVR treats these reports as confidential to sponsors and does not make them available for general circulation. Individual sponsors may, however, authorize subsequent release of the material.

UNIVERSITY OF SOUTHAMPTON

INSTITUTE OF SOUND AND VIBRATION RESEARCH

DYNAMICS GROUP

Sources of Error and Confidence Intervals for SEA Parameters of Two Coupled Rectangular Plates

by

W.S. Park, D.J. Thompson and N.S. Ferguson

ISVR Technical Memorandum No. 856

December 2000

Authorized for issue by
Dr. M.J. Brennan
Group Chairman

CONTENTS

1. INTRODUCTION

Many engineering structures have complex geometric and physical properties which are subject to statistical uncertainties. For a specific set of values of these properties, the finite element and boundary element methods can give a deterministic solution at low frequencies. As the frequencies of interest increase, large computation effort may be needed to obtain good accuracy. In general, such a model can not represent real structures because it is merely one member of an ensemble and the results are valid for that model only. Due to statistical uncertainties of the geometric and physical properties there is little value in detailed information. Thus simple methods giving qualitative characteristics need to be developed.

Such an alternative approach is to use statistical energy analysis (SEA) which is widely used in the noise and vibration field to study structures, such as spacecraft, ships, buildings and automotive vehicles. SEA is a powerful technique in which structures are characterised at high frequencies and high modal overlap using only a few global parameters for each subsystem, e.g. the mode count, the damping loss factor, the coupling loss factor (CLF) and the input power. There are, however, many uncertainties and potential errors in using SEA, as for example Fahy and Mohammed [1-2] and Mace [3] have investigated.

The CLF, which is used to define the transmission of energy from one subsystem to another, is one of the most important parameters used in SEA. It should be realised that it is a statistical quantity. The "actual" CLF is defined in terms of an ensemble average and as such it is not uncertain once this ensemble of systems is defined. However, the "effective" CLF for a given realisation (member of the ensemble) differs from the statistical average.

Once the subsystems have been defined and the respective CLFs are correctly obtained, then SEA is very straightforward. However, there are many methods, numerical, analytical or experimental, to evaluate the CLF. Conventionally the CLF between two structures, such as two plates, is obtained by analysing the wave transmission for semi-infinite structures [4-6] or by a modal approach [5]. Finite Element Analysis has also been used to study the CLF for specific systems at low modal overlap by several authors [7-9]. The CLF obtained from the wave approach generally overestimates the actual value at low frequencies (low modal overlap). Significant fluctuations with frequency are also observed in this low frequency region.

This report presents the direct evaluation of the "effective" CLF through the use of the dynamic stiffness method (DSM) to obtain the dynamic response of finite structures expressed in terms of the power balance equation [10]. The structures considered are two coupled rectangular plates, with two opposite edges simply supported. Initially some preliminary results are also given for a single rectangular plate. Although a number of studies of a two plate system have previously been performed, most of them have been limited to plates of the same thickness [1, 2, 7, 8]. The effect of varying the ratio of plate thicknesses is considered here as part of a parameter study.

2. THEORY

2.1 SEA Theory

In the SEA approach, a system is modelled in terms of the power which is input, dissipated and transmitted between subsystems. The power balance equations for two conservatively coupled subsystems 1 and 2 excited separately one at a time, as illustrated in Figure 2.1, can be expressed by [5]

$$\overline{P}^1_{1,\text{in}} = \overline{P}^1_{1,\text{diss}} + \overline{P}^1_{12} = \omega\left(\eta_1 \overline{E}^1_1 + \eta^1_{12}\overline{E}^1_1 - \eta^1_{21}\overline{E}^1_2\right) \tag{2.1}$$

$$0 = \overline{P}^1_{2,\text{diss}} + \overline{P}^1_{21} = \omega\left(\eta_2 \overline{E}^1_2 + \eta^1_{21}\overline{E}^1_2 - \eta^1_{12}\overline{E}^1_1\right) \tag{2.2}$$

$$\overline{P}^2_{2,\text{in}} = \overline{P}^2_{2,\text{diss}} + \overline{P}^2_{21} = \omega\left(\eta_2 \overline{E}^2_2 + \eta^2_{21}\overline{E}^2_2 - \eta^2_{12}\overline{E}^2_1\right) \tag{2.3}$$

$$0 = \overline{P}^2_{1,\text{diss}} + \overline{P}^2_{12} = \omega\left(\eta_1 \overline{E}^2_1 + \eta^2_{12}\overline{E}^2_1 - \eta^2_{21}\overline{E}^2_2\right) \tag{2.4}$$

where P_{in} and P_{diss} are the time-averaged input and dissipated powers, P_{12} (= -P_{21}) is the net power transmitted from subsystem 1 to 2, η_1 and η_2 are the internal loss factors, E_1 and E_2 are the total time-averaged energies, and η_{12} and η_{21} are the coupling loss factors. The superscript, 1 or 2, means the excitation is applied to subsystem 1 or 2 and " ¯ " denotes an ensemble averaged quantity. The "actual" CLFs are defined in terms of this ensemble average. The equations (2.1) - (2.4) also hold for individual realisations, in which case the CLFs are replaced by $\hat{\eta}_{ij}$, the "effective" CLF.

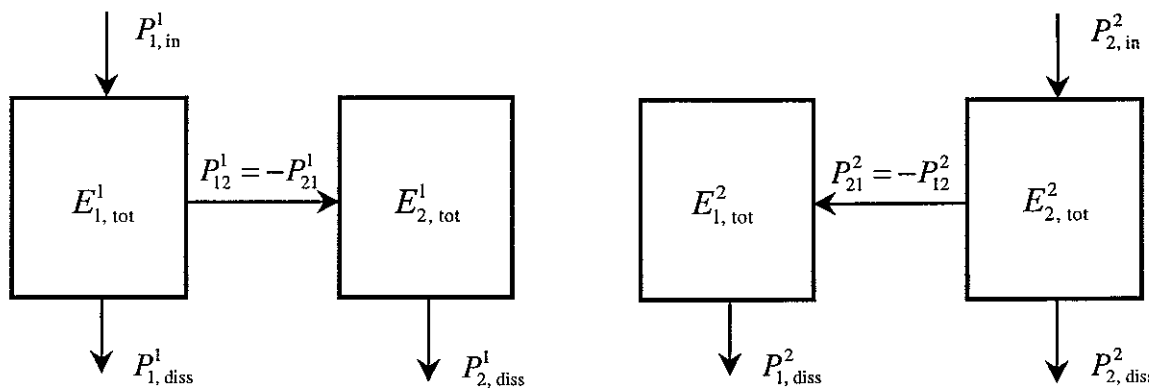

Figure 2.1. Two subsystem model

Equations (2.1)-(2.2) and (2.3)-(2.4) can be rearranged to give,

$$\overline{P}^1_{1,\text{in}} = \overline{P}^1_{1,\text{diss}} + \overline{P}^1_{2,\text{diss}} \tag{2.5}$$

$$\overline{P}^2_{2,\text{in}} = \overline{P}^2_{1,\text{diss}} + \overline{P}^2_{2,\text{diss}} . \tag{2.6}$$

Equations (2.5) and (2.6) are always correct and do not assume any relationships between the transmitted power and the average subsystem energies. Accordingly, the input power for each subsystem is equal to the sum of the dissipated powers for the two subsystems. The net coupling powers are equal to the dissipated powers of the receiver subsystems.

$$\overline{P}^1_{12} = \overline{P}^1_{2,\text{diss}} \tag{2.7}$$

$$\overline{P}^2_{21} = \overline{P}^2_{1,\text{diss}} . \tag{2.8}$$

Equations (2.1)-(2.4) can be used to obtain the CLFs from input powers and subsystem energies. In general $\eta^1_{ij} \neq \eta^2_{ij}$, the four equations allowing solution for these four unknowns (if η_1 and η_2 are known). However the usual SEA assumption is that $\eta^1_{ij} = \eta^2_{ij}$. Moreover it is usually assumed that the CLFs are related to one another by

$$n_1 \eta_{12} = n_2 \eta_{21} \tag{2.9}$$

where n_1 and n_2 are the asymptotic modal densities of the subsystems. This is derived from the fundamental assumption in SEA, that the coupling power is proportional to the difference in average modal energy, *i.e.* $P_{12} \propto \omega(E_1/n_1 - E_2/n_2)$, the constant of proportionality being $n_1 \eta_{12}$ [11].

If the time-averaged input power, the time-averaged energy and the internal loss factor for both subsystems are known, the "effective" CLF $\hat{\eta}_{ij}$ may be evaluated by using the power balance equations (2.1) and (2.3) (assuming $\hat{\eta}^1_{ij} = \hat{\eta}^2_{ij}$)

$$\begin{Bmatrix} \hat{\eta}_{12} \\ \hat{\eta}_{21} \end{Bmatrix} = \omega \begin{bmatrix} E^1_1 & -E^1_2 \\ -E^2_1 & E^2_2 \end{bmatrix}^{-1} \begin{Bmatrix} P^1_{1,\text{in}} - \omega\eta_1 E^1_1 \\ P^2_{2,\text{in}} - \omega\eta_2 E^2_2 \end{Bmatrix} . \tag{2.10}$$

From equations (2.5)-(2.8), the right-hand terms of equation (2.10) are equivalent to

$$P_{1,\text{in}}^1 - \omega\eta_1 E_1^1 = P_{1,\text{in}}^1 - P_{1,\text{diss}}^1 = P_{12}^1 \tag{2.11}$$

and

$$P_{2,\text{in}}^2 - \omega\eta_2 E_2^2 = P_{2,\text{in}}^2 - P_{2,\text{diss}}^2 = P_{21}^2. \tag{2.12}$$

Therefore the "effective" CLF for a particular realisation of the system is given by

$$\begin{Bmatrix} \hat{\eta}_{12} \\ \hat{\eta}_{21} \end{Bmatrix} = \omega \begin{bmatrix} E_1^1 & -E_2^1 \\ -E_1^2 & E_2^2 \end{bmatrix}^{-1} \begin{Bmatrix} P_{12}^1 \\ P_{21}^2 \end{Bmatrix}. \tag{2.13}$$

This is the same concept as performing "experimental" SEA based on the power injection method [12]. Alternatively, exciting only one subsystem and using the reciprocity relation (2.9), the CLF can be obtained from

$$\hat{\eta}_{12} = \frac{P_{12}}{\omega\left\{E_1 - \frac{N_1}{N_2}E_2\right\}} \quad \text{or} \quad \hat{\eta}_{12} = \frac{P_{12}}{\omega\left\{E_1 - \frac{n_1(\omega)}{n_2(\omega)}E_2\right\}} \tag{2.14), (2.15}$$

where N_1 and N_2 are the actual number of modes in a given frequency band and $n_1(\omega)$ and $n_2(\omega)$ are the asymptotic modal densities. For example, the modal density of a simply supported uniform isotropic plate can be approximated as [4]

$$n(\omega) = \left(\frac{S}{4\pi}\right)\left(\frac{\rho h}{D}\right)^{1/2} \tag{2.16}$$

where S is the area of plate, ρ is the material density, h is the thickness of plate and $D\left(=\frac{Eh^3}{12(1-\nu^2)}\right)$ is the flexural rigidity. It can be expected that equations (2.13) - (2.15) will give different estimates of $\hat{\eta}_{ij}$. This will be evaluated in section 4.1.

2.2 Analytical result for CLF

For two-dimensional subsystems coupled along a line, the CLF can be estimated from analytical results for semi-infinite structures [4]

$$\eta_{12\infty} = \frac{c_{g1} L_{12} \tau_{12}}{\pi \omega S_1} \tag{2.17}$$

where c_{g1} is the group velocity of subsystem 1, L_{12} is the junction length, τ_{12} is the power transmission coefficient or the transmission efficiency, which is the ratio of transmitted power to incident power, and S_1 is the surface area of the source subsystem. If the incident wave is a bending wave on a homogeneous thin plate then the group velocity $c_g = 2c_b$, where c_b is the phase velocity of the bending wave. The transmission efficiency τ_{12} is the angular averaged value. It is usual to assume a diffuse field, so that τ_{12} is given by [4]

$$\tau_{12,\mathrm{d}} = \int_0^{\pi/2} \tau_{12}(\theta) \cos\theta \, d\theta \tag{2.18}$$

where θ is the angle of incidence. The transmission efficiency $\tau_{12}(\theta)$ for two plates joined at right angles with identical material properties is given by [4]

$$\tau_{12}(\theta) = \frac{2\psi\sqrt{\chi^2 - s^2}\sqrt{1 - s^2}}{\psi^2 + \psi\left(\sqrt{\chi^2 + s^2}\sqrt{1 + s^2} + \sqrt{\chi^2 - s^2}\sqrt{1 - s^2}\right) + \chi^2} \tag{2.19}$$

where $\chi = \sqrt{h_1/h_2}$, $\psi = (h_2/h_1)^2$ and $s = \sin(\theta)$. The transmission efficiency τ_{12} can also be expressed in terms of the angular averaged transmission loss R_{12}, an approximate formula for which is given by [6]

$$R_{12} = -10\log_{10}(\tau_{12}) \simeq 20\log_{10}\left[\left(\frac{\chi}{\psi}\right)^{1/2} + \left(\frac{\psi}{\chi}\right)^{1/2}\right] + C_1 + \frac{C_2}{\chi} + C_3 \log_{10}\left[1 + \frac{1}{\chi^4}\right] \tag{2.20}$$

where C_1 = -2.0053, C_2 = 0.2535 and C_3 = 1.56. These transmission efficiencies and the CLF results for semi-infinite plates are described in more detail in Appendix A.

2.3 Theoretical upper and lower limits for CLF

For a finite structure, η_{ij} will differ from $\eta_{ij\infty}$. Moreover, for a particular realisation of a structure, $\hat{\eta}_{ij}$ will differ from η_{ij}, particularly at low modal overlap. Craik *et al.* [13] observed that the fluctuations with frequency at low modal overlap in the energy level difference, which

is related to the CLF, closely match the fluctuations in the spatially averaged point mobility of the receiver subsystem. An empirical expression for the CLF at any frequency is given as [13]

$$\hat{\eta}_{12} = \eta_{12\infty} \frac{\mathrm{Re}(Y_2)}{\mathrm{Re}(Y_{2\infty})} \tag{2.21}$$

where $\eta_{12\infty}$ is the CLF for semi-infinite structures, Y_2 is the spatially-averaged point mobility for the receiver subsystem and $Y_{2\infty}$ is the point mobility of the equivalent infinite system.

Although no derivation of this is given in [13], the relation between the spatially-averaged point mobility and the coupling loss factor can be seen from the fact that the modal density can be expressed by [5]

$$n(\omega) = 2m\,\mathrm{Re}(Y_\infty)/\pi \tag{2.22}$$

where m is the total mass. The reciprocity relationship (2.9) can thus be written as

$$\eta_{12}\,\mathrm{Re}(Y_{1\infty})m_1 = \eta_{21}\,\mathrm{Re}(Y_{2\infty})m_2 . \tag{2.23}$$

The real part of the spatially-averaged point mobility can be found by summing the contribution from all modes given as [4, 5]

$$\mathrm{Re}(Y(\omega)) = \sum_i \left[\omega_i \eta m \left\{ 1 + \left(\frac{\omega_i}{\omega} - \frac{\omega}{\omega_i} \right)^2 \frac{1}{\eta^2} \right\} \right]^{-1} \tag{2.24}$$

where ω_i is the resonance frequency of the ith mode. If the response is dominated by a single mode, the peak mobility $\hat{Y}$, where ω equals ω_i, is given by

$$\hat{Y} = \frac{1}{\omega_i \eta m} \tag{2.25}$$

which is real.

Thus the ratio of the peak mobility for a finite system $\hat{Y}$ to the real part of the mobility for the equivalent infinite system Y_∞ is obtained from equations (2.22) and (2.25)

$$\frac{\hat{Y}}{\mathrm{Re}(Y_\infty)} = \frac{2}{\pi \omega_i \eta n(\omega)} = \frac{2}{\pi M} \tag{2.26}$$

where M ($=\omega\eta n(\omega)$) is the modal overlap factor. This is the height of the resonance maxima above the characteristic mobility (defined as the geometric mean between the resonance peaks and the anti-resonance minima) given by [14].

For a frequency band, the maximum value of the frequency average mobility $<\hat{Y}>$ can be approximated by [4]

$$\left\langle \hat{Y} \right\rangle = \frac{1}{m\Delta\omega} \tan^{-1}\left(\frac{\Delta\omega}{\eta\omega_i} \right) \tag{2.27}$$

where $\Delta\omega$ is a frequency band. When $\Delta\omega/\eta\omega_i$ is very small (high damping, low frequency, or a narrow frequency band for the analysis), then $<\hat{Y}>/\mathrm{Re}(Y_\infty)$ is the same as equation (2.26). However, if $\Delta\omega/\eta\omega_i$ is large (such as for a one-third octave band containing many modes), $\tan^{-1}(\Delta\omega/\eta\omega_i)$ is approximately $\pi/2$, and then

$$\frac{\left\langle \hat{Y} \right\rangle}{\mathrm{Re}(Y_\infty)} = \frac{1}{n\Delta\omega} = \frac{1}{N} \tag{2.28}$$

where N is the number of modes in a specific frequency band. This gives the upper limit for the ratio of the actual CLF to the semi-infinite result, from equation (2.21),

$$\frac{(\hat{\eta}_{ij})_{\max}}{\eta_{ij\infty}} = \frac{1}{N}. \tag{2.29}$$

The minimum value for the mobility has been given by [14, 15], considering the contributions of all mode pairs,

$$\breve{Y} = \frac{\mathrm{Re}(Y_\infty)}{\beta} \tag{2.30}$$

where

$$\beta = \frac{2}{\pi\eta\omega}\frac{d\omega}{dN} = \frac{2}{\pi M}. \tag{2.31}$$

If we consider a two-mode approximation, this anti-resonance mobility becomes

$$\breve{Y} = \frac{\mathrm{Re}(Y_\infty)}{\beta}\frac{8}{\pi^2} = Y_\infty \frac{4M}{\pi}. \tag{2.32}$$

Therefore, the lower limit for the CLF ratio is given by Craik *et al.* [13] as

$$\frac{(\hat{\eta}_{ij})_{min}}{\eta_{ij\infty}} = \frac{4M}{\pi}. \tag{2.33}$$

These relations will be compared in Chapter 5 with simulations for a two plate system.

2.4 Calculation of energies of coupled plates based on the Dynamic Stiffness Method

In the present study, to obtain the energies and powers in equations (2.1 and 2.3), the dynamic response of a two plate system is obtained by using the dynamic stiffness method (DSM) [10, 16-18]. This gives an analytical solution which is valid over a wide frequency range. The main disadvantage is that it can only be used for particular continuous elements. For plate structures, these must be simply supported on two opposite edges which must be parallel. The dynamic properties of a structural component are determined exactly in the form of a frequency-dependent dynamic stiffness matrix. The equations of motion of coupled subsystems can then be solved to yield the dynamic response of the structure. In the current analysis, the in-plane motion of longitudinal and shear waves as well as the out-of-plane motion is considered, since bending waves and in-plane waves can be coupled at the joint between the two plates. The use of the DSM for two coupled plates was presented in reference [10].

Since a point force excites components of vibration with different numbers of half-wavelength n across the plate width, a study was performed [10] to establish how many components should be included to achieve convergence of the solution. The maximum number of Fourier components n_{max} is chosen such that all components with cut-on frequencies lower than the frequency band considered are included [10]. The cut-on frequency of waves with Fourier component n is given by

$$f_{cut\text{-}on} = \frac{\pi}{2}\left(\frac{n}{b}\right)^2\left(\frac{D}{\rho h}\right)^{1/2} \tag{2.34}$$

where b is the width of plate, $D\left(=Eh^3/12(1-\nu^2)\right)$ is the bending stiffness, ρ is the material density and h is the thickness of plate.

The time-averaged input power can be calculated by

$$P_{\text{in}} = 1/2\ \text{Re}\{\, F^{*} v \,\} \tag{2.35}$$

where F is the applied harmonic force amplitude, v is the velocity amplitude at the driving point and * denotes the complex conjugate. The dissipated power can be determined from

$$P_{\text{diss}} = \eta \omega E \tag{2.36}$$

where E is the energy of the subsystem.

The strain energy for flexural vibration is given by [10]

$$U_f = \frac{D}{2}\int_0^b \int_0^L \left[\left(\frac{\partial^2 w}{\partial x^2} \right)^2 + \left(\frac{\partial^2 w}{\partial y^2} \right)^2 + 2\nu \frac{\partial^2 w}{\partial x^2}\frac{\partial^2 w}{\partial y^2} + 2(1-\nu)\left(\frac{\partial^2 w}{\partial x \partial y} \right)^2 \right] dxdy \tag{2.37}$$

and that for in-plane vibration is given by [10]

$$U_i = \frac{1}{2}\frac{Eh}{1-\nu^2}\int_0^b \int_0^L \left[\left(\frac{\partial u}{\partial x} \right)^2 + \left(\frac{\partial v}{\partial y} \right)^2 + 2\nu \frac{\partial u}{\partial x}\frac{\partial v}{\partial y} + \frac{(1-\nu)}{2}\left(\frac{\partial u}{\partial y} + \frac{\partial v}{\partial x} \right)^2 \right] dxdy . \tag{2.38}$$

In calculating the energy of each plate, a numerical integration is performed. A step size between sampled points of 1/6 of the bending wavelength at the maximum frequency is found to give good agreement, with an error of less than 1 % [10].

The transmitted power, P_{12}, is obtained directly from,

$$P_{12} = \frac{1}{2}\text{Re}\left[\sum_n \int_0^b F_n^{*}(y)\{ j\omega w_n(y) \} dy \right] \tag{2.39}$$

where F_n is the internal force amplitude at the interface calculated from the dynamic stiffness matrix and w_n is the displacement amplitude, calculated for each Fourier component n, integrated along the interface length, and then summed. Account is taken of both forces and moments at the interface.

3. VALIDATION OF MODELS

This report concentrates on the power flow between two coupled plates. Initially, however, some results are given for a single plate to validate the numerical accuracy or the correctness of the formulation.

3.1 A single plate

As a preliminary study, validation was performed for a single plate model to examine the input and dissipated powers. The single plate, as shown in Figure 3.1, is assumed to be simply supported along two opposite longitudinal edges ($y = 0$ and $y = b$) in order to apply the DSM.

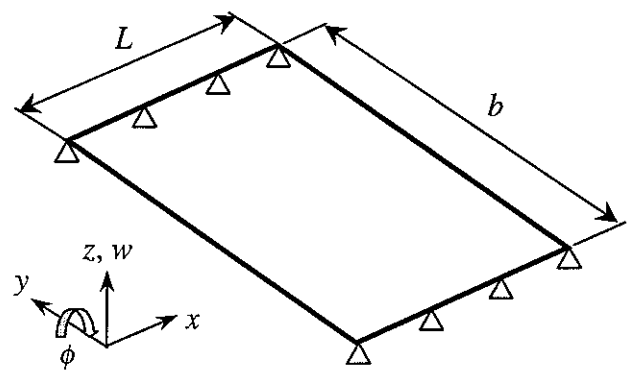

Figure 3.1. A single plate: width $b = 1.0$ m, length $L = 0.5$ m, thickness $h = 3.0$ mm, material: aluminium (Young's modulus $E = 7.24\times10^{10}$ N/m^2, Poisson's ratio $\nu = 0.333$, material density $\rho = 2794$ kg/m^3).

3.1.1 Validation of the input power calculation for a finite plate

The input power, when a point force is applied at the centre of the left-hand edge ($x = 0$), was calculated by equation (2.35) (see section 2.4) and compared with that for a semi-infinite plate excited on its edge. For a harmonic force of amplitude F, the time-averaged input power for the semi-infinite plate is given by

$$P_{in\infty} = \frac{1}{2}|F|^2 \,\mathrm{Re}\left\{\frac{1}{Z_\infty}\right\} \tag{3.1}$$

where Z_∞ is the impedance of the semi-infinite plate [4, 19] corrected by [20]

$$Z_\infty \cong 2.165\sqrt{D\rho h} \tag{3.2}$$

and Re denotes the real part. Note that Z_∞, and hence $P_{in\infty}$, is independent of frequency. The calculated input power for the single plate converges, as expected, to that for the semi-infinite plate at high frequencies, as shown in Figure 3.2.

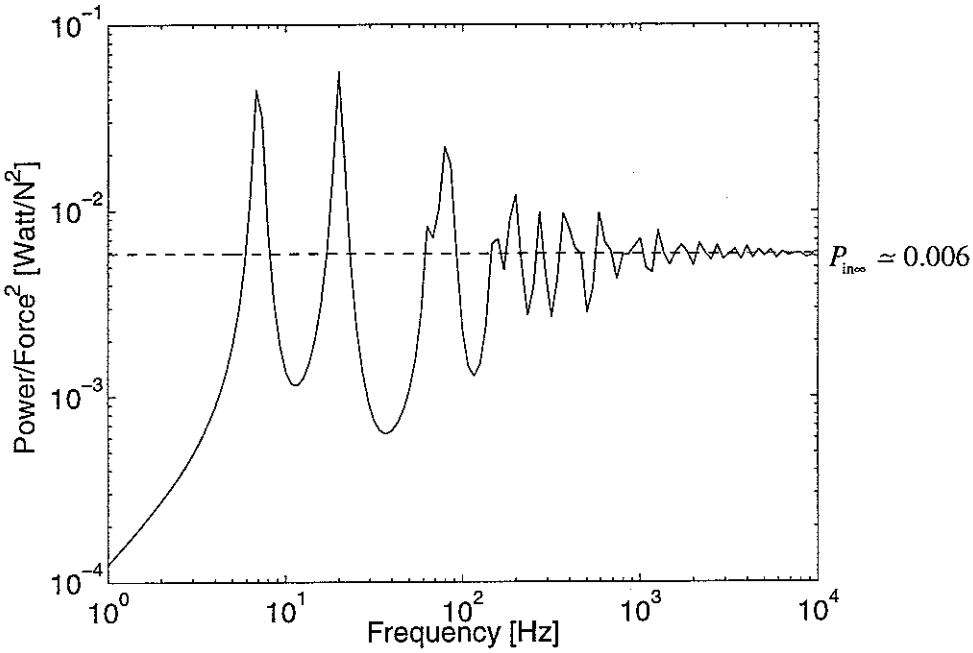

Figure 3.2. Comparison of the input power for the single plate (the damping loss factor $\eta = 0.1$) with that for the semi-infinite plate when a point force is applied at the centre of the left-hand edge; —, finite plate; ---, semi-infinite plate.

3.1.2 Estimates of dissipated power based on strain and kinetic energy

If losses are from material damping, the maximum strain energy in a cycle should be used in evaluating the dissipated power [10],

$$P_{\text{diss}} = \eta\omega E_{\text{strain}} \tag{3.3}$$

from the definition of the loss factor given by [4]

$$\eta = \frac{\text{energy lost per cycle}}{2\pi\,(\text{reversible mechanical energy})} = \frac{P_{\text{diss}}}{\omega E}. \tag{3.4}$$

Often, especially in experimental SEA, the maximum kinetic energy in a cycle is used to estimate the dissipated power,

$$P_{\text{diss}} \cong \eta\omega E_{\text{kin}} \tag{3.5}$$

as it is a quantity more amenable to measurement. This relies on the equality [15]

$$E_{\text{kin}} \cong E_{\text{strain}} \cong E \tag{3.6}$$

where E is the time averaged total energy. This is satisfied in a broad-band sense, but not necessarily at single frequencies except at the natural frequencies.

In a steady state, the power balance between the predicted input power and the predicted dissipated power should be satisfied. To investigate whether this is the case, the single plate (Figure 3.1) was considered with a point force applied at the centre of the left-hand edge. Figure 3.3 compares the input power with the dissipated power, the latter calculated from either the strain or kinetic energy. The right-hand figures show the error in each case, and are plotted against modal overlap factor, $M = \eta\omega\, n(\omega)$, rather than frequency.

This shows that if the kinetic energy is used to calculate the dissipated power, the error in regions of low modal overlap is very large. The error decreases as the frequency increases due to the higher modal overlap. On the other hand, the error produced when using the strain energy is extremely small, within about $\pm$ 1 %, and these powers coincide very well. The remaining error is due to the numerical integration. Thus, it is clear that the strain energy should be used when the dissipated power is evaluated in the low and mid frequency range, whereas the kinetic energy is widely used because of simplicity, both experimentally and analytically. It should be remarked that the current simulations use a damping model in which losses are introduced by making the Young's modulus complex. In practical structures other damping mechanisms may be present, such as friction at joints, which may be more related to kinetic energy rather than strain energy.

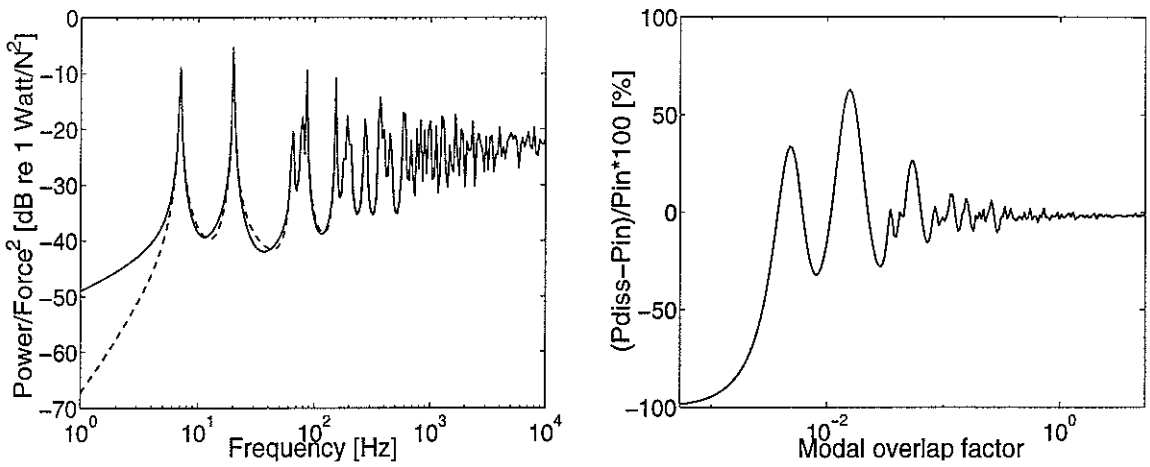

(a) Power obtained from kinetic energy and its error

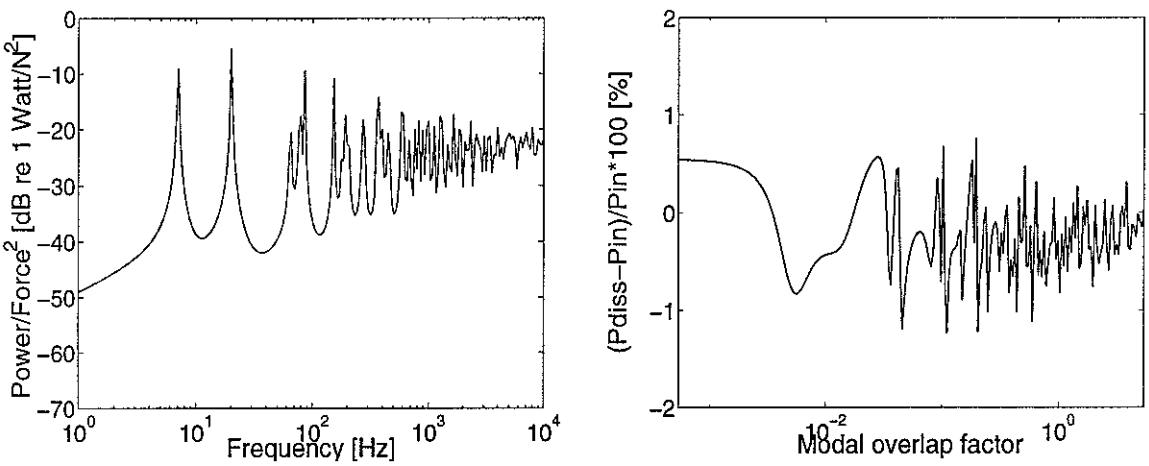

(b) Power obtained from strain energy and its error

Figure 3.3. The comparison of the predicted input power with the dissipated power and their error calculated from (a) kinetic energy and (b) strain energy for a single plate model (the damping loss factor $\eta = 0.01$); —, the input power; ---, the dissipated power.

3.2 Two coupled plates with a point force applied along an edge

Two rectangular plates are considered, coupled at right angles, as shown in figure 3.4, and simply supported along the longitudinal edges ($y = 0$ and $y = b$). A point force is applied first at the centre of left-hand edge ($x_1 = 0$) of plate 1 and then at the right-hand edge ($x_2 = L_2$) of plate 2, in each case perpendicular to the plate surface.

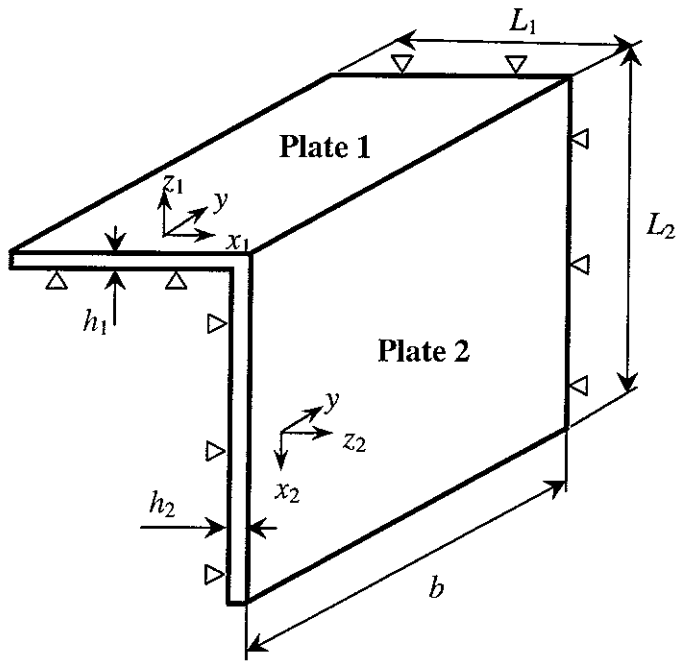

Figure 3.4. Two perpendicular plates: width $b = 1.0$ m, length $L_1 = 0.5$ m, $L_2 = 1.0$ m, thickness $h_1 = 3.0$ mm, $h_2 = 2.0$ mm, the damping loss factor $\eta_1 = \eta_2 = 0.1$, material: aluminium (Young's modulus $E = 7.24\times10^{10}$ N/m^2, Poisson's ratio $\nu = 0.333$, material density $\rho = 2794$ kg/m^3).

3.2.1 The power balance for two coupled plates

The input and total dissipated powers for the two plates as described in equations (2.5-2.6), are shown in Figure 3.5. Here only flexure is considered, in-plane motion being suppressed. These powers were evaluated at frequencies spaced equally on a logarithmic scale such that three points are contained in each one-third octave band. The results are then converted to one-third octave bands. The input and dissipated powers coincide very well, within less than ± 1 %.

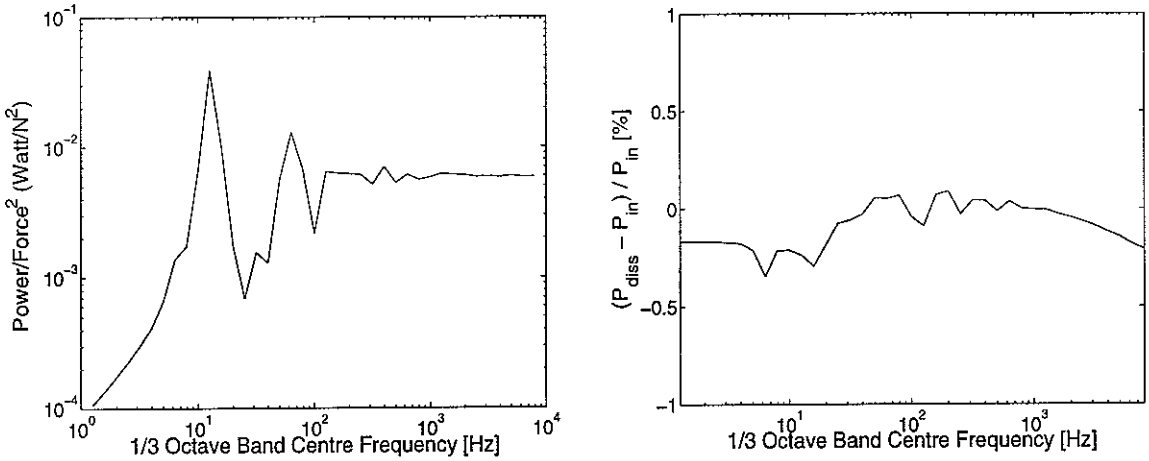

(a) The input power; —, when a harmonic force is applied at the centre of the left-hand edge of plate 1 and the dissipated power; ---, and the error between them.

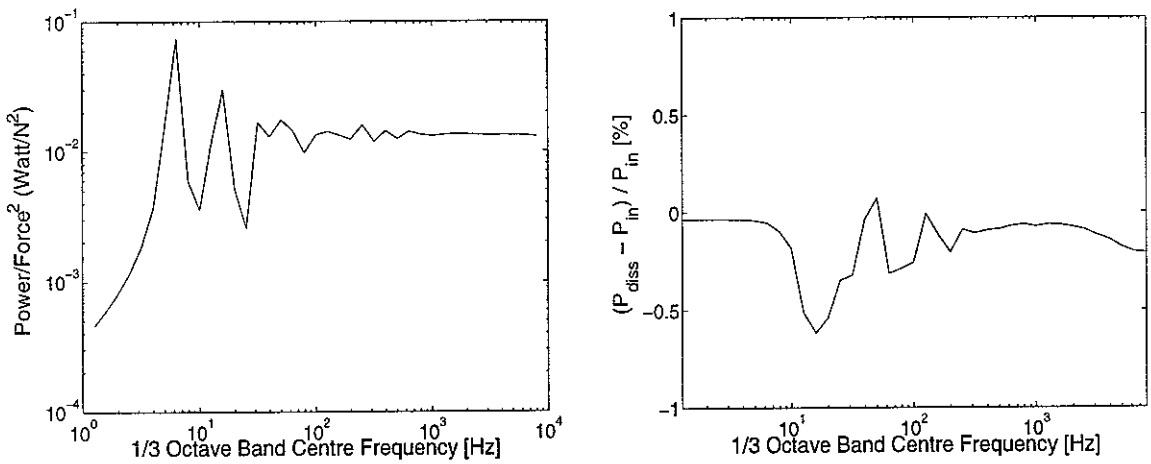

(b) The input power; —, when a harmonic force is applied at the centre of the right-hand edge of plate 2 and the dissipated power; ---, and the error between them.

Figure 3.5. The predicted input power and the dissipated power for the two coupled plates.

3.2.2 The dissipated power for the receiver plate and the coupling power

The coupling power from the source plate to the receiver plate can be obtained by the internal force and moment extracted from the dynamic stiffness matrix at their interface using equation (2.37). This coupling power should be equal to the power dissipated in the receiver plate (equations 2.7 and 2.8), as the coupling is conservative. The predicted power dissipated for the receiver plate and the coupling power are presented in Figure 3.6. The coupling power for each

location of the applied force, on plate 1 or on plate 2, coincides well with the power dissipated for the respective receiver plate. As above, the error is less than ± 1 % in the range considered.

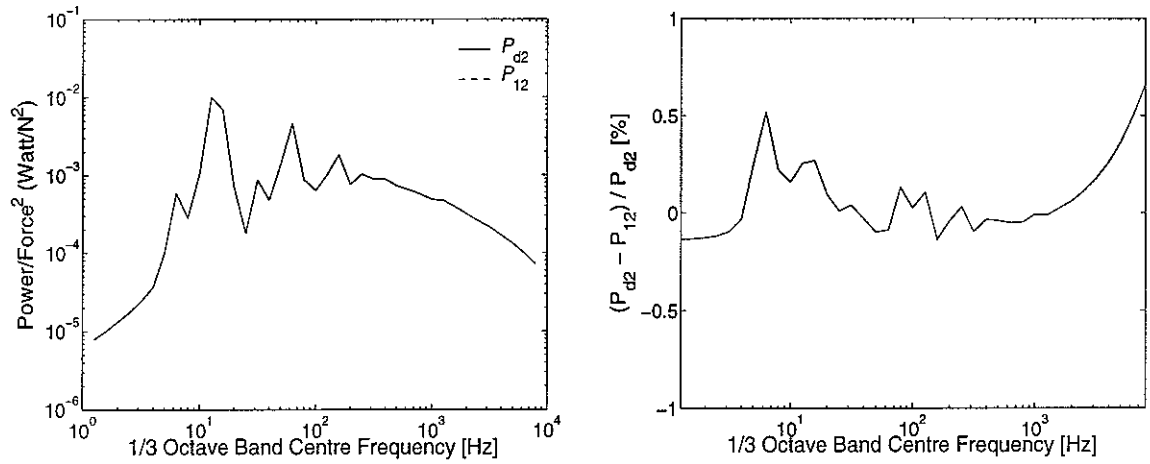

(a) The dissipated power for plate 2 for excitation on plate 1; —, P_{d2}, and the coupling power; ---, P_{12}, and the error between them.

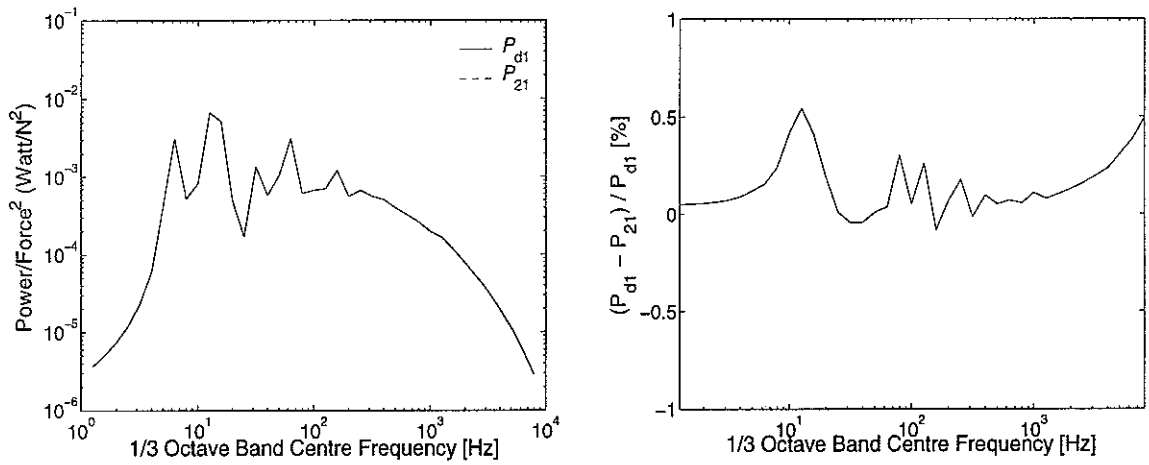

(b) The dissipated power for plate 1 for excitation on plate 2; —, P_{d1}, and the coupling power; ---, P_{21}, and the error between them.

Figure 3.6. The dissipated power for the receiver plate and the coupling power between two plates.

3.2.3 The effect of in-plane vibration

The results shown previously have neglected the effect of in-plane motion and considered only flexural motion of the plates. This section describes the results obtained when in-plane motion is included in the full formulation of the dynamic stiffness matrix [10]. For the two perpendicular plates (Figure 3.4), a harmonic force is again applied at the centre of the left-hand edge of plate 1 or the right-hand edge of plate 2, in each case in a direction perpendicular to the plate surface. Figure 3.7 shows the ratio of the time-averaged strain energies in the two plates, with and without in-plane motion. From this it can be seen that the inclusion of in-plane motion has only a small effect for the present case. In fact, it is negligible up to the cut-on frequency of the shear wave propagation for the receiver plate, which is found to be 872 Hz for plate 1 and 1188 Hz for plate 2. This cut-on frequency of in-plane vibrations for the receiver plate was examined by using the dynamic stiffness matrix which included in-plane motion. The natural frequencies of the in-plane motion for different dimensions are shown in Table 3.1. The first frequencies correspond to the cut-on frequency of the in-plane shear mode. Above that frequency, a small amount of flexural energy from the source plate is transmitted into in-plane energy in the receiver plate, through their common edge. Although the effect of in-plane vibrations on the two coupled plates considered here is small, it may be important for multi-plate structures, as investigated by Bercin [21].

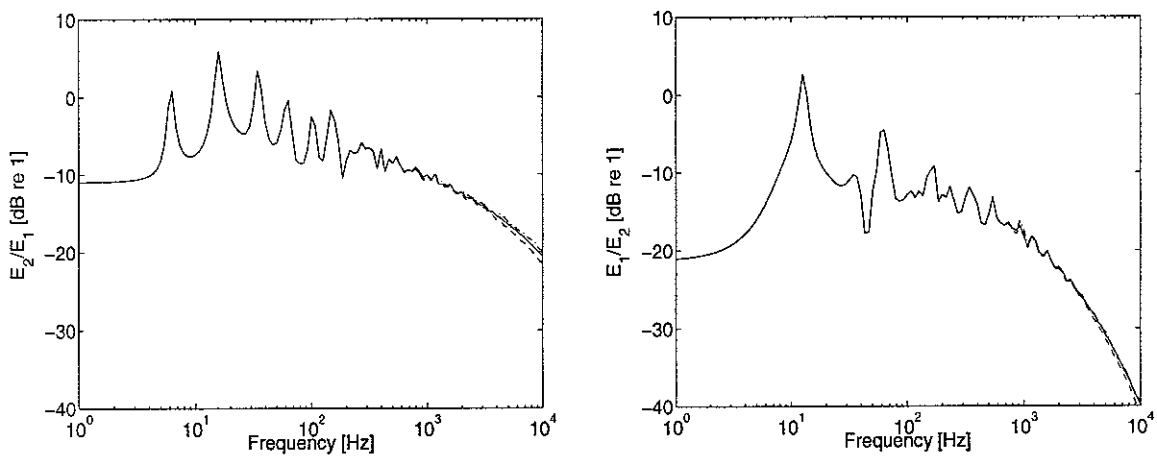

(a) $E_{\text{plate2}} / E_{\text{plate1}}$ (b) $E_{\text{plate1}} / E_{\text{plate2}}$

Figure 3.7. The effect of in-plane motion on the time-averaged strain energy ratio for the perpendicular plates when a harmonic force is applied (a) at the centre of the left-hand edge, $x_1 = 0$, of plate 1 (b) at the centre of the right-hand edge, $x_2 = L_2$, of plate 2; —, flexure only; --- ; with in-plane (flexural energy); -·-, with in-plane (total).

Table 3.1. The natural frequencies of in-plane vibrations for the receiver plate.

Length L_2 [m]	Width b [m]	Thickness h_2 [mm]	Natural frequencies [Hz]
0.3	1.0	2.0	608.1, 2530
0.5	1.0	2.0	867.6, 2509
1.0	1.0	2.0	1188, 2203, 2899
2.0	1.0	2.0	1368, 1571, 2203
4.0	1.0	2.0	1423, 1440, 1695, 1932
0.5	1.0	3.0	871.8, 2501

3.3 Two coupled plates with an internal point force applied to one plate

To model a harmonic point force applied inside one plate, the source plate is separated into two parts at the longitudinal position of the applied force, as shown in Figure 3.8. Actually this system has three plates, two directly excited plates and one receiver plate. The global dynamic stiffness matrix of this system can be assembled using the transformation matrix [10]. The point force is applied no closer than 1/4 of the bending wavelength at the maximum frequency from the edge in order to avoid nearfield effects. This model will be used to evaluate the effective CLF, the confidence intervals and various parameter studies. In these calculations the force point is located at a range of different positions to simulate 'rain-on-the-roof' excitation. For each forcing point the source plate has to be subdivided at the corresponding x coordinate.

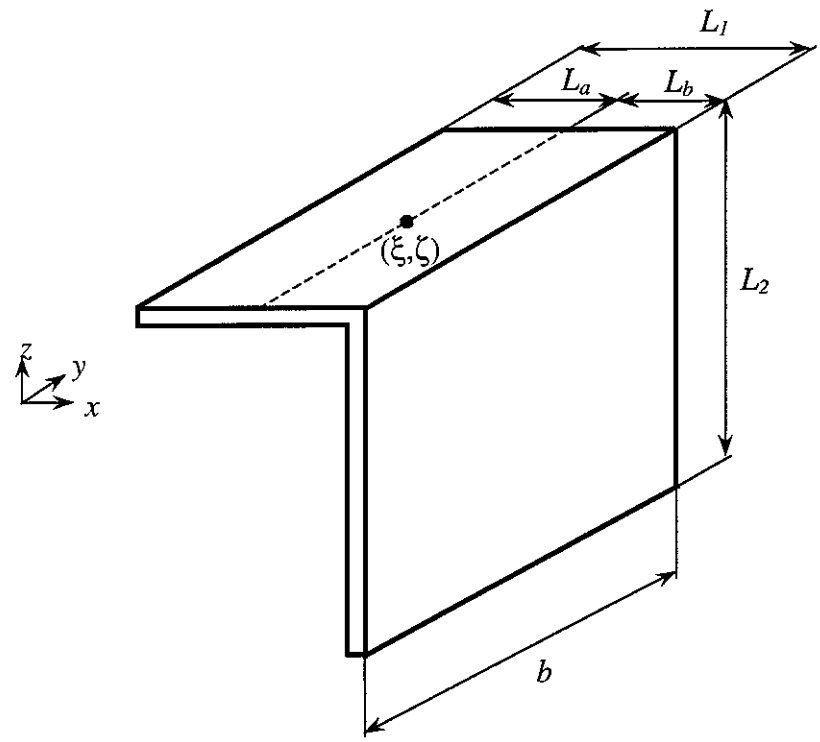

Figure 3.8. Two perpendicular plates with a point force applied inside one plate: width b = 1.0 m, length $L_1 = 0.5$ m, $L_2 = 1.0$ m, thickness $h_1 = 3.0$ mm, $h_2 = 2.0$ mm, the damping loss factor $\eta_1 = \eta_2 = 0.1$, material: aluminium (Young's modulus $E = 7.24\times10^{10}$ N/m^2, Poisson's ratio $\nu = 0.333$, material density $\rho = 2794$ kg/m^3).

4. CLF AND RECIPROCITY

4.1 The evaluation of CLFs using different methods

As described in section 2.1, there are a number of methods to evaluate the CLF; these are compared here. By exciting one plate and taking account of the actual number of modes in each frequency band, or using the asymptotic modal densities of the plates, the CLF can be calculated by using equation (2.14) or (2.15) respectively. The actual number of modes in each frequency band has been obtained from the determinant of the inverse of the dynamic stiffness matrix of each individual uncoupled plate for the various Fourier components n. The mode count for the two uncoupled plates is presented in Figure 4.1. These are summarised in Table 4.1 - 4.2. A simply supported boundary condition is imposed at the edge normally joined to the other plate.

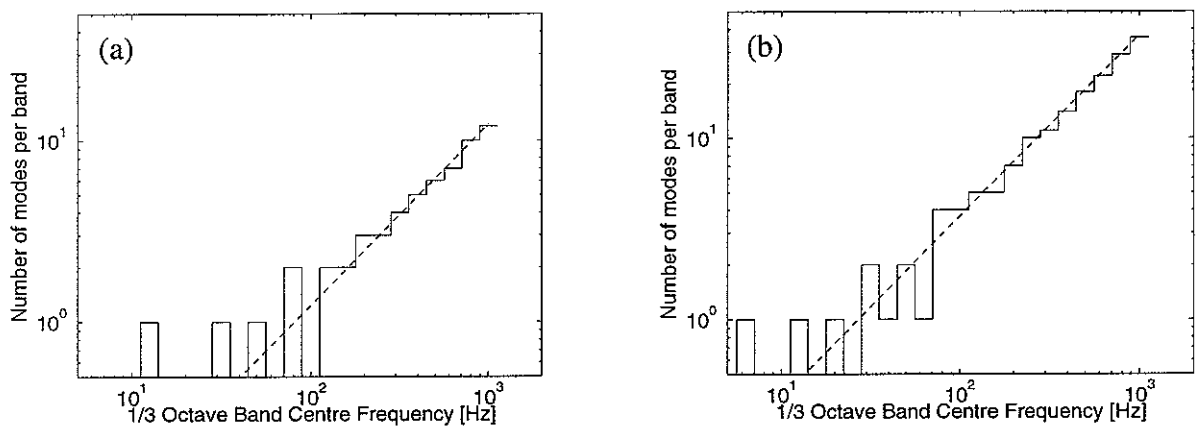

Figure 4.1. The mode count for two uncoupled plates; (a) plate 1 and (b) plate 2; —, the number of modes counted from the "frequency function" (*i.e.* det $(\mathbf{K}^{-1}) = 0$); ---, asymptotic modal density from equation (2.16).

Alternatively, the CLF can be directly evaluated by using equation (2.13), in which case each plate has to be excited in turn. These results have been calculated with 400 randomly selected forcing points on each plate, which will be explained further in Section 4.5. The input power, transmitted power and dissipated power are calculated at discrete frequencies (three per 1/3 octave band) and averaged into 1/3 octave bands before applying equations (2.13-15). The results of these three methods are compared in Figure 4.2 with the conventional CLF estimate obtained from the wave transmission approach on semi-infinite plates, $\eta_{ij\infty}$, equation (2.17).

Table 4.1. The number of modes for plate 1 (0.5 m ×1.0 m, h_1 = 3mm) with 3 simply supported edges and one free edge in each 1/3 octave frequency band from $n = 1$ to 12: f_l = lower frequency, f_c = centre frequency, f_u = upper frequency of band.

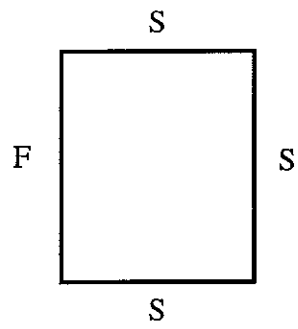

S : simply supported edge

F : free edge

f_l	f_c	f_u	1	2	3	4	5	6	7	8	9	10	11	12	sum
5.62	6.3	7.08													
7.08	8	8.91													
8.91	10	11.2													
11.2	12.5	14.1	1												1
14.1	16	17.8													
17.8	20	22.4													
22.4	25	28.2													
28.2	31.5	35.5		1											1
35.5	40	44.7													
44.7	50	56.2	1												1
56.2	63	70.8													
70.8	80	89.1		1	1										2
89.1	100	112													
112	125	141			1	1									2
141	160	178	1			1									2
178	200	224		1	1		1								3
224	250	282				1	1	1							3
282	315	355	1	1			1	1							4
355	400	447			1	1		1	2						5
447	500	562	1	1			1		1	2					6
562	630	708			1	1		1	1	1	2				7
708	800	891	1	1	1		1	1		1	1	2	1		10
891	1000	1120				1	1	1	1	1	1	2	2	2	12

Table 4.2. The number of modes for plate 2 (1.0 m ×1.0 m, h_2 = 2mm) with 3 simply supported edges and one free edge in each 1/3 octave frequency band from $n = 1$ to 15: f_l = lower frequency, f_c = centre frequency, f_u = upper frequency of band.

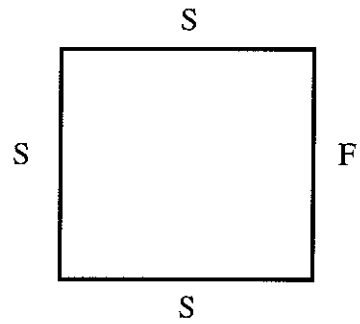

S : simply supported edge

F : free edge

f_l	f_c	f_u	1	2	3	4	5	6	7	8	9	10	11	12	13	14	15	sum
4.47	5	5.62																
5.62	6.3	7.08	1															1
7.08	8	8.91																
8.91	10	11.2																
11.2	12.5	14.1	1															1
14.1	16	17.8																
17.8	20	22.4		1														1
22.4	25	28.2																
28.2	31.5	35.5	1	1														2
35.5	40	44.7			1													1
44.7	50	56.2		1	1													2
56.2	63	70.8	1															1
70.8	80	89.1		1	1	2												4
89.1	100	112	1	1	1	1												4
112	125	141	1		1	1	2											5
141	160	178		1		1	2	1										5
178	200	224	1	1	1	1	1	2										7
224	250	282	1	1	1	1	1	2	3									10
282	315	355	1	1	1	1	1	1	2	3								11
355	400	447	1	1	1	1	1	2	2	2	3							14
447	500	562	1	1	2	1	2	1	1	2	3	4						18
562	630	708	1	1	1	2	1	2	2	2	2	3	4	1				22
708	800	891	2	2	1	1	2	1	2	2	2	2	3	5	4			29
891	1000	1120	1	1	2	2	2	2	2	2	2	2	3	3	4	6	2	36

The calculated CLFs agree well with the semi-infinite result $\eta_{ij\infty}$ in the high frequency range. At low frequencies, the predicted CLFs fluctuate considerably relative to $\eta_{ij\infty}$. The results based on the mode count and the modal density coincide closely, although there are some negative or non-available values omitted from the graph. These occur due to numerical problems in some frequency bands where no resonant modes of either plate exist. Negative CLFs, mentioned and investigated in [7, 12], may be attributed to the non-resonant response. This means that the energy of the receiver plate, at a particular frequency, can be greater than that of the source plate, as can be seen from Figure 3.7 when E_2 / E_1 rises above 0 dB. Accordingly, the "numerical experiment" result, from equation (2.13), turns out to be a more reliable method than the others and does not usually produce negative values. The remaining results in this report will be based on this latter method.

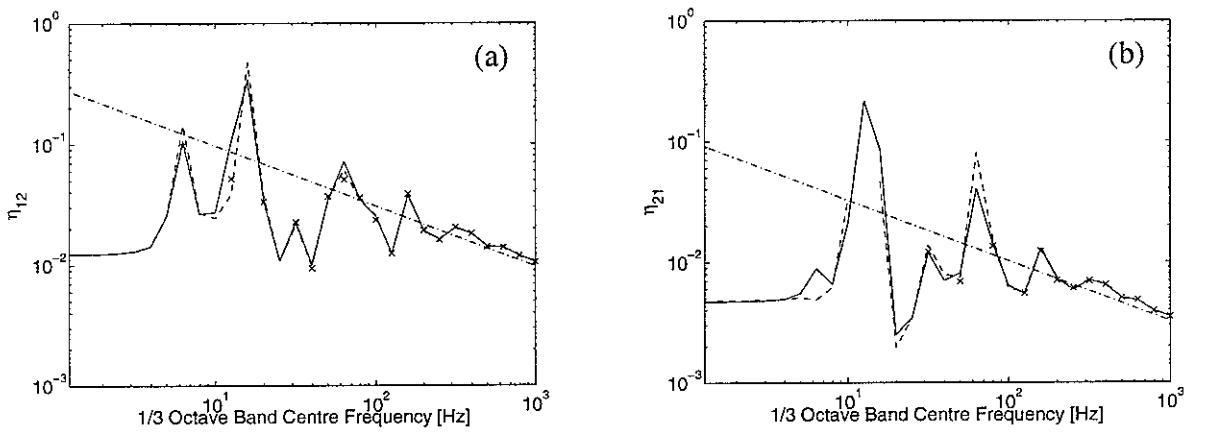

Figure 4.2. Comparison of CLFs (a) $\hat{\eta}_{12}$ (b) $\hat{\eta}_{21}$ obtained from several methods; ××, from mode count (equation 2.14); – –, from modal density (equation 2.15); —, "numerical experiment" (equation 2.13); –·–, semi-infinite plates (equation 2.17).

4.2 The CLF and its relationship to the energy ratio and the global/local modes

This section illustrates the relationships between the CLF and the energy ratio of two subsystems and the effect of the modal characteristics of the receiver plate, which, according to Craik, *et. al.* [13], is the reason for fluctuation in the coupling of two subsystems. The ratio between the energy of the receiver plate and that of the source plate is shown in Figure 4.3. The upper figures show results when plate 1 is excited while the lower figures correspond to excitation of plate 2. In each case 400 forcing points are used. If the energy of the receiver plate is greater than that of the source plate or not much less, a peak is found in the respective

energy ratio. These peaks correspond to peaks in the CLF in Figure 4.2. Over nearly all one third octave bands, the receiver plate has a lower energy level than the source plate, see Figures 4.3 (c) and (d).

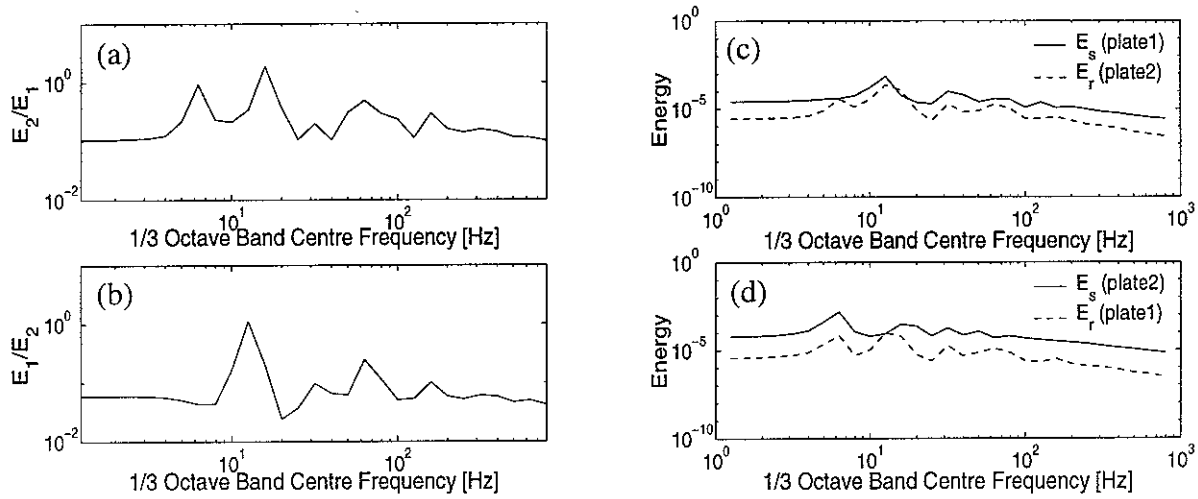

Figure 4.3. The ratio between the energy of the receiver plate and that of the source plate and the energy of each plate; (a) and (c): plate 1 - the source plate, plate 2 - the receiver plate, (b) and (d): plate 2 - the source plate, plate 1 - the receiver plate.

The energy results are related to the global modes of the coupled plates, especially the peaks in the energy ratio occurring at lower frequencies, where global modes may occur (see Figure 4.3 (a) and (b)). Figure 4.4 shows the frequency response function for the two plate system (a) and the uncoupled plates (b and c) with each plate simply supported at the joint. In Figure 4.4 (a), the first and third peaks at approximately 6 Hz and 14 Hz result in peaks in the energy ratio when plate 1 is excited (see Figure 4.3 (a)) and in $\hat{\eta}_{12}$ (see Figure 4.2 (a)). These peaks correspond to the two resonances of the uncoupled plate 2 (see Figure 4.4 (c)). The second peak, at approximately 12 Hz, results in a peak in the energy ratio when plate 2 is excited (see Figure 4.3 (b) and in $\hat{\eta}_{21}$ (see Figure 4.2 (b)). This 12 Hz peak corresponds to first resonance of plate 1 (see Figure 4.4 (b)). Thus the CLF estimates at low frequencies, which correspond to the first few modes, are dominated by the uncoupled modes of the receiver plate. It is also possible that the source plate may also affect the CLF. This will be investigated further in a subsequent study.

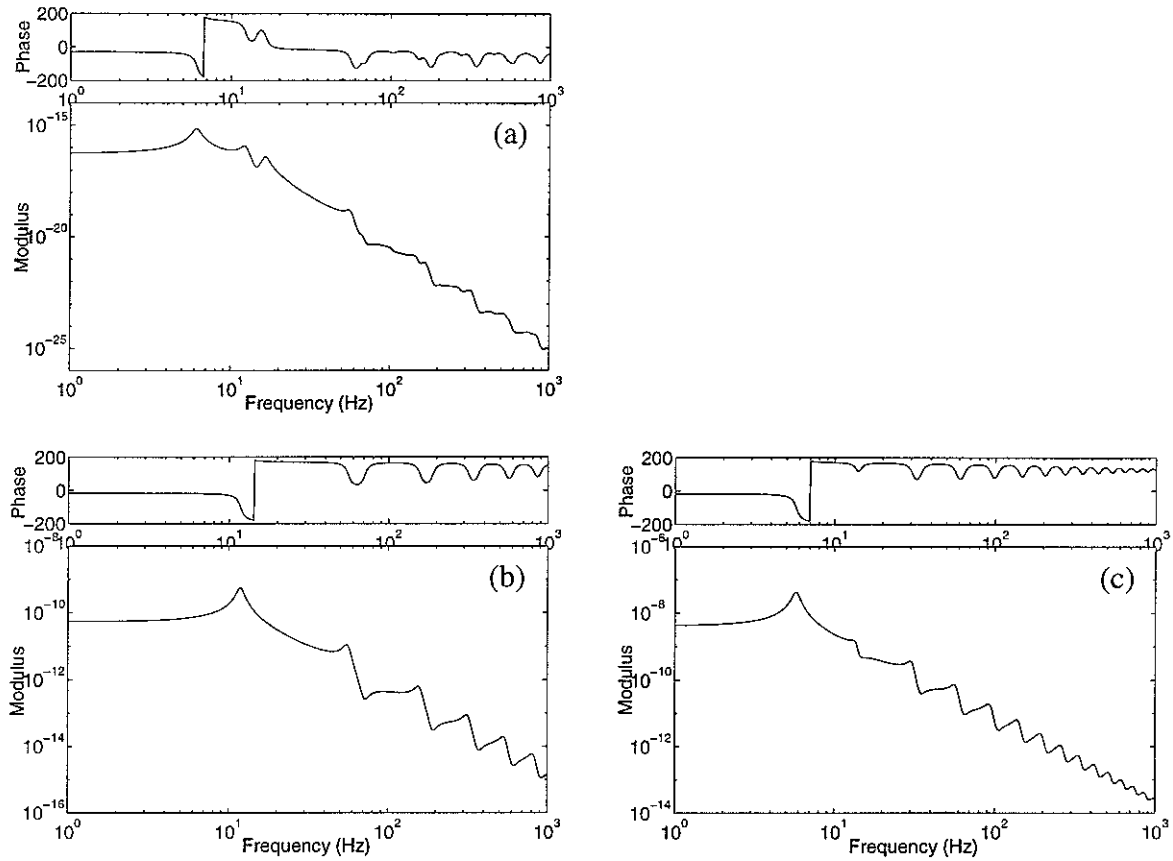

Figure 4.4. Frequency response functions for the two plate system (a) and the uncoupled plate with 3 simply supported edges and one free edge ((b) plate 1 and (c) plate 2), for the Fourier component $n = 1$. Peaks correspond to modes.

4.3 Effect of plate thickness on high frequency asymptotic behaviour

In the previous sections the results obtained for two finite plates were compared with equivalent results obtained for two semi-infinite plates, and it was shown that the results converged at high frequencies (see Figure 4.2). Nevertheless some discrepancies remained. In this section the results are compared at high frequencies for a range of plate thicknesses. Plate 1 is fixed at $h_1 = 3$ mm and plate 2 is varied between $h_2 = 0.949$ and $h_2 = 9.49$ mm.

In order to compare these results for finite and infinite plates more readily it is more convenient to express them in terms of a transmission efficiency τ_{ij} rather than a coupling loss factor η_{ij}. The reason for this choice is that τ_{ij} is independent of frequency and also of plate dimensions (other than thickness). The equivalence between the two parameters is given by equation (2.17) for the infinite plate case. Here equation (2.17) is used in reverse to infer an equivalent transmission efficiency τ for the finite plates. The finite plate results comprise the average over the frequency range 400 - 4000 Hz, to give an approximation to the high frequency asymptotic behaviour. The finite plate simulations are based on two square plates with width $b = 1$ m and length $L = 1$ m, joined at a right angle. In-plane motion is not included in this section. The infinite plate results are the angular averaged transmission efficiency for a right angle joint (see [4] and Appendix A).

Figure 4.5 compares the results. Although good agreement is found for dissimilar thicknesses, there is a discrepancy when $h_1 \simeq h_2$.

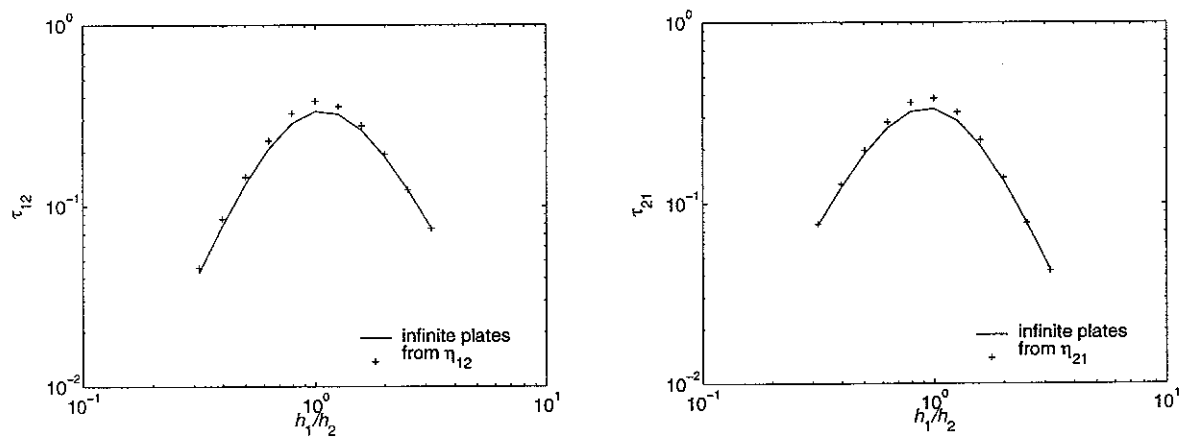

Figure 4.5. Comparison of the transmission efficiencies for finite plates with the angular averaged transmission efficiency defined by equation (2.18); —, the angular averaged transmission efficiency, + +, the transmission efficiency obtained for finite plates.

If the angular averaged transmission efficiency for the infinite plate, τ, is corrected by a factor of $2/(2-\tau)$ (see [22] and Appendix A), it coincides well with that obtained for the finite plates, as presented in Figure 4.6. This correction is one which needs to be applied to the transmission efficiency for infinite plates in determining coupling loss factors. It allows for the fact that, when τ is large, the average energy of the source plate depends on τ as a large proportion of the power incident on the boundary is transmitted, whereas if τ is small the reflected and incident energies are approximately equal.

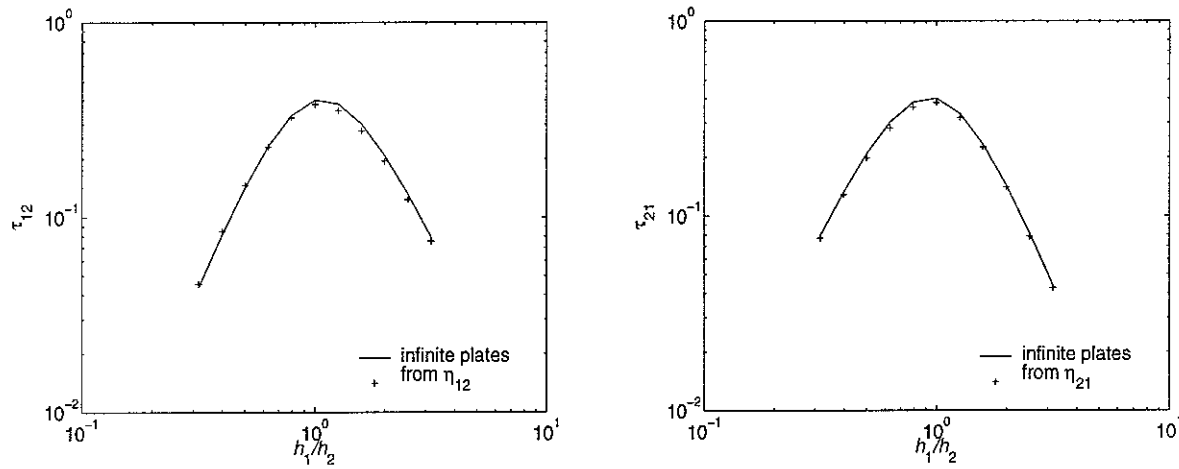

Figure 4.6. Comparison of the transmission efficiencies for finite plates with the corrected angular averaged transmission efficiency [22]; —, the corrected angular averaged transmission efficiency $2\tau/(2-\tau)$, + +, the transmission efficiency obtained for finite plates.

The remaining discrepancy seen in Figure 4.2 (and later for other thickness ratios) can be attributed to the inclusion of in-plane motion in the finite plate results and its neglect in $\eta_{ij\infty}$.

4.4 Reciprocity relationship

The reciprocity relationship, described in equation (2.9), is not assumed in the "numerical experiment" method of equation (2.13). The difference between $n_1\hat{\eta}_{12}$ and $n_2\hat{\eta}_{21}$ was examined and the result is presented in Figure 4.7. The ratio $n_2\hat{\eta}_{21}/n_1\hat{\eta}_{12}$ for the two coupled finite plates fluctuates at low frequencies and converges to 1, as expected, as frequency increases.

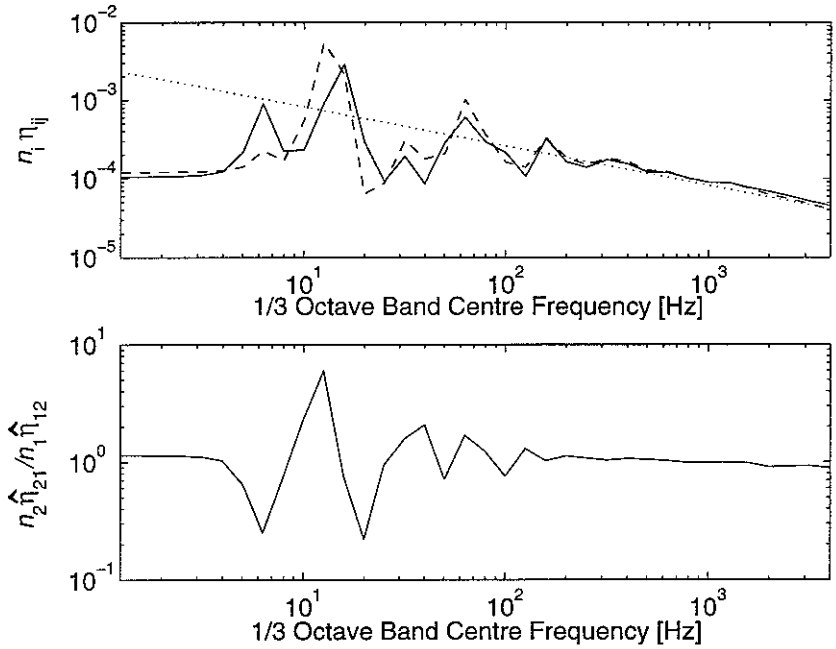

Figure 4.7. Comparison of the reciprocity relationship for two coupled plates obtained from numerical experiment and with that for plates using the semi-infinite plate coupling loss factors; —, $n_1\hat{\eta}_{12}$; ---, $n_2\hat{\eta}_{21}$; ..., $n_1\eta_{12\infty}$ and $n_2\eta_{21\infty}$. n_1 and n_2 are the asymptotic modal densities of plate 1 and plate 2 obtained from equation (2.16).

4.5 The sensitivity to number and location of forcing points

In SEA it is usually assumed that the forcing of each subsystem is of the 'rain-on-the-roof' or 'delta-correlated' form. To simulate this, a total of 400 point forces have been used, applied individually first on plate 1, then on plate 2. For numerical convenience, these were chosen at 20 random y co-ordinates, the same for each of 20 random x co-ordinate positions. All points are chosen to exclude an area at the edge of the plate within 1/4 of the bending wavelength at the maximum frequency. These forces are uncorrelated, and are assumed to have an identical broad-band spectrum.

An investigation has been performed into the variability in the results obtained for different numbers of forcing points. As the number increases, the solution should converge. This investigation was performed for the two plate system of Figure 3.8. Results were obtained, for 400 forcing points as shown in Figure 4.8. These were then grouped into sets of different sizes and the CLFs were determined from equation (2.13) using the energies and the dissipated powers due to each set of forcing points. For example, using 50 sets of 8 forcing points gave 50 estimates of CLF which were calculated by 8 forcing points randomly selected from the 400 available. These CLF estimates were then used to determine confidence intervals. In order to avoid bias in the results, no overlapping sets were taken. Results were calculated for 400 sets of 1 forcing point, 100 sets of 4 forcing points, 50 sets of 8 forcing points, 20 sets of 20 forcing points, 10 sets of 40 forcing points and 8 sets of 50 forcing points.

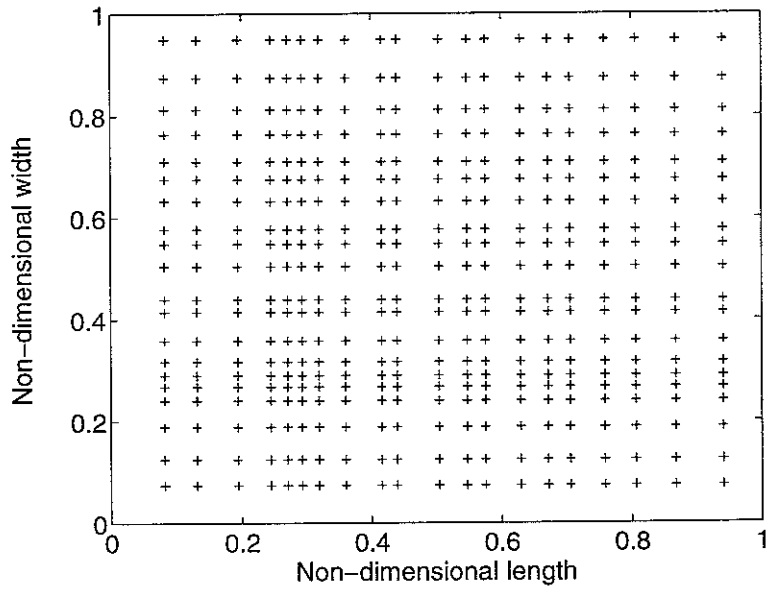

Figure 4.8. Forcing points applied in plate 1

The confidence intervals were examined for these 6 different sized sets of forcing points. Figure 4.9 shows the mean values and 95% confidence intervals for these different sets. It can be seen that the confidence intervals are large for small numbers of forcing points and reduce as more points are taken. They are not strongly dependent on frequency.

Figure 4.10 shows the range of the 95% and 67% confidence intervals relative to the mean value, for three particular frequency bands (100, 500Hz and 1kHz). This shows, for example, that using a single excitation point (set size of 1) can be expected to introduce an uncertainty of up to 10 dB (*i.e.* ± 5 dB) in the CLF. As the number of forcing points increases, the CLF estimates become more reliable, so that for a 95% confidence interval of ± 1 dB at least 10 points should be taken.

Figure 4.11 shows the variation of the mean values of the effective CLFs for these 6 different set sizes. The mean value of the effective CLF for 400 sets of 1 is systematically higher at low frequencies, but the differences become small as the set size increases.

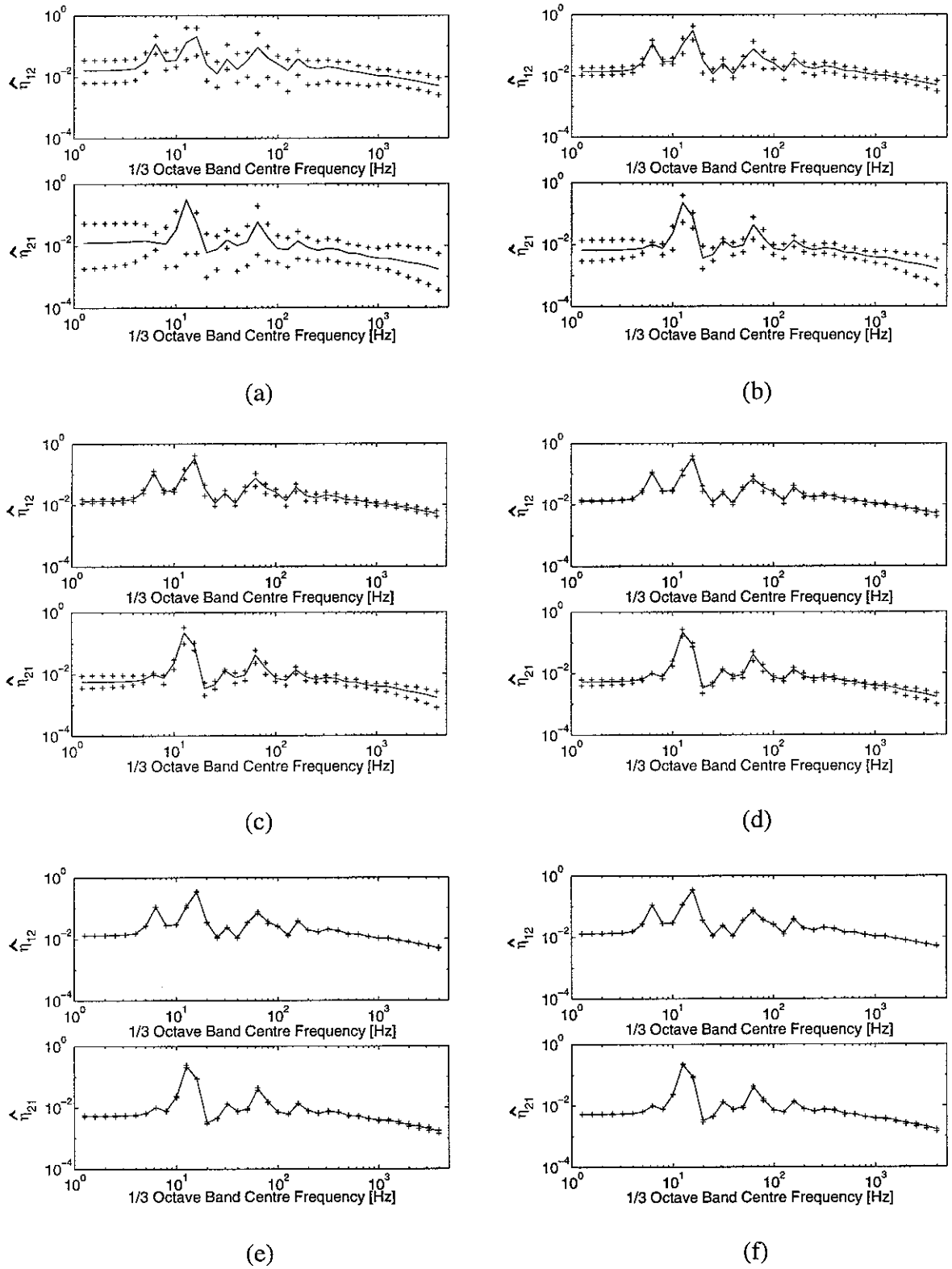

Figure 4.9. The mean values and 95% confidence intervals for the effective CLFs; (a) 400 sets of 1, (b) 100 sets of 4, (c) 50 sets of 8, (d) 20 sets of 20, (e) 10 sets of 40 and (f) 8 sets of 50; —, mean CLF; -+-, 95% confidence interval.

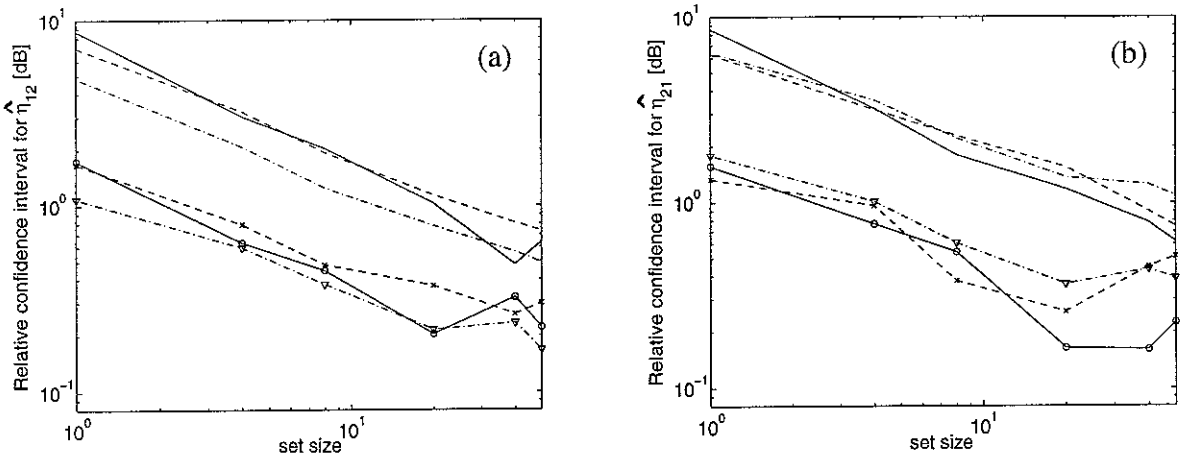

Figure 4.10. Relative 95% and 67% confidence intervals, (a) $\hat{\eta}_{12}$ and (b) $\hat{\eta}_{21}$, for different number of forcing points, 400 sets of 1, 100 sets of 4, 50 sets of 8, 20 sets 20, 10 sets of 40 and 8 sets of 50 at three different frequencies; —, 95% at 100 Hz; ---, 95% at 500 Hz; –·–, 95% at 1 kHz; -o-, 67% at 100 Hz; -x-, 67% at 500 Hz; -Δ-, 67% at 1 kHz.

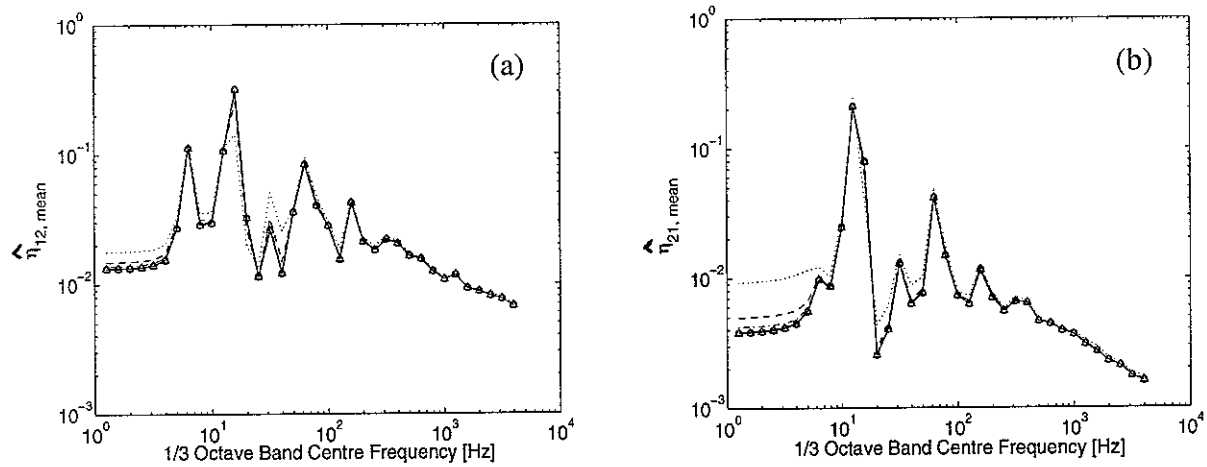

Figure 4.11. The mean values of the CLFs, (a) $\hat{\eta}_{12,\,mean}$ and (b) $\hat{\eta}_{21,\,mean}$, for different number of forcing points; ..., 400 sets of 1; ---, 100 sets of 4; –·–, 50 sets of 8; ___, 20 sets 20; -Δ-, 10 sets of 40; -o-, 8 sets of 50.

5. PARAMETER STUDY

A sensitivity analysis has been performed here using the DSM model described above to evaluate the influence of the following parameters: the plate thickness ratio, h_1/h_2, the length ratio, L_1/L_2, the length to width ratio of the two plates L_1/b and the damping loss factors, $\eta_1 = \eta_2$. In the calculations, the dimensions of plate 1 ($L_1 = 0.5$ m, $b = 1$ m, $h_1 = 3$ mm) are kept fixed and the relevant dimensions of plate 2 are given 11 logarithmically spaced values between 0.3 and 3 times that for plate 1. The values considered for the damping loss factor are 0.03, 0.1 and 0.3. A similar parameter study was considered by Boisson *et al.* [23] although they did not evaluate the CLF but the energy ratio between two plates. Their results showed only the minima and maxima of the energy ratio as a quantitative description of the frequency dependence.

The results of this study are shown in Figures 5.1-5.4 in terms of the ratio between the effective CLF $\hat{\eta}_{ij}$ for finite plates and the semi-infinite plate result $\eta_{ij\infty}$. These results are plotted against the modal overlap factor for the source plate, that for the receiver plate, and the geometric mean modal overlap factor, $M_{12} = (M_1 M_2)^{1/2}$. Since the dimensions of plate 1 are kept fixed, the results versus M_1 correspond to a fixed frequency range, 1.87 to 1870 Hz, for all receiver plates. Also shown, at low modal overlap, are estimates of upper and lower bounds, equations (2.29, 2.33), as given by Craik *et al.* [13]. These are based on the appropriate value of modal overlap factor, M_1, M_2 or M_{12}.

Figure 5.1 shows the CLF ratio, obtained by varying the thickness ratio, against the relevant modal overlap factor. At low modal overlap, the first peak in the CLF ratio corresponds approximately to the cut-on frequency for the receiver plate, as described in section 4.2. As the thickness of plate 2 decreases, its cut-on frequency decreases since it is proportional to the square root of the thickness of the plate, and the first peak moves to the left (see Figure 5.1 (a) $\hat{\eta}_{12}/\eta_{12\infty}$). For $\hat{\eta}_{21}/\eta_{21\infty}$, the first peak moves to the right, since the modal density of the source plate (M_2) is inversely proportional to the square root of the thickness of this plate although the cut-on frequency of plate 1 is kept fixed (see Figure 5.1 (a) $\hat{\eta}_{21}/\eta_{21\infty}$). On the contrary, when plotted against the modal overlap factor for the receiver plate, the peaks are roughly fixed although the thickness of plate 2 decreases (see Figure 5.1 (b)). This can be identified from the

definition of the cut-on frequency and that of the modal density, equations (2.16) and (2.34), *i.e.* $f_{\text{cut-on}} \propto h^{1/2}$ and $n(\omega) \propto h^{-1/2}$.

If the thicknesses of the plates do not vary but the lengths vary, the cut-on frequency for each case is the same, since it is independent of the length of the plate. However, the peaks move to lower frequencies as the length is increased, since the modal density is proportional to the area of the plate, as shown in Figure 5.2 (a) - (b). If the width of the plate is varied, it affects the modal density, $n \propto S$ $(= L\,b)$, as well as the cut-on frequency, $f_{\text{cut-on}} \propto 1/b^2$, of the source or receiver plate. Thus the peaks move to the right for every case in Figure 5.3 as the width of the plate b is reduced. Figure 5.4 shows the CLF ratios for different damping loss factors. As the damping loss factors of both plates increase, the variation in the effective CLF becomes small.

In general, for modal overlap greater than 1, the variation in the effective CLF is small, although the effective CLF does not always converge to that for the semi-infinite plate as the latter does not take into account the in-plane vibrations. At low modal overlap most of the results fluctuate considerably and fall within the bounds described in section 2.3. The percentage of the values falling within these bounds has been investigated, discounting results below the first resonance of either plate, and is shown in Tables 5.1-5.2. When the CLF ratio is plotted against the geometric mean modal overlap factor M_{12}, this shows better agreement than that against the modal overlap factor for the source or receiver plate. Virtually all of the results fall within the slightly wider range $\eta_{\min} / 3 < \hat{\eta}_{ij} < 3\eta_{\max}$ (the upper and lower bounds $\pm$ 5dB).

There are two things under investigation here; one is the validity of the Craik's upper and lower bounds and the other is to determine whether the variability in the CLF depends on the modal properties of the source subsystem, the receiver subsystem, or both the source and receiver subsystems. It appears from the results presented that Craik's upper and lower bounds are a useful measure of variability in the CLF, although the best agreement occurs when modal overlap of both subsystems is taken into account rather than that of the receiver as proposed by Craik. These issues will be studied further in a subsequent report.

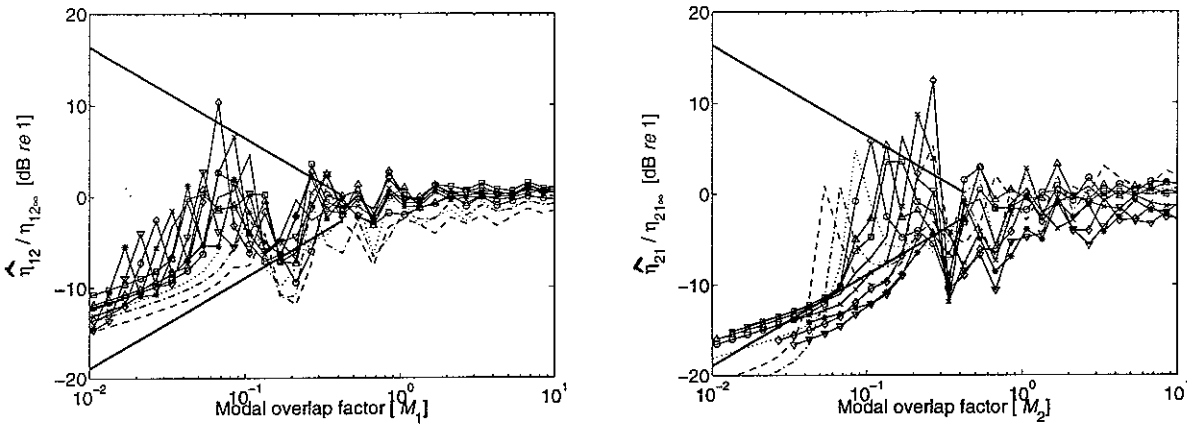

(a) the CLF ratio plotted against the modal overlap factor for the source plate

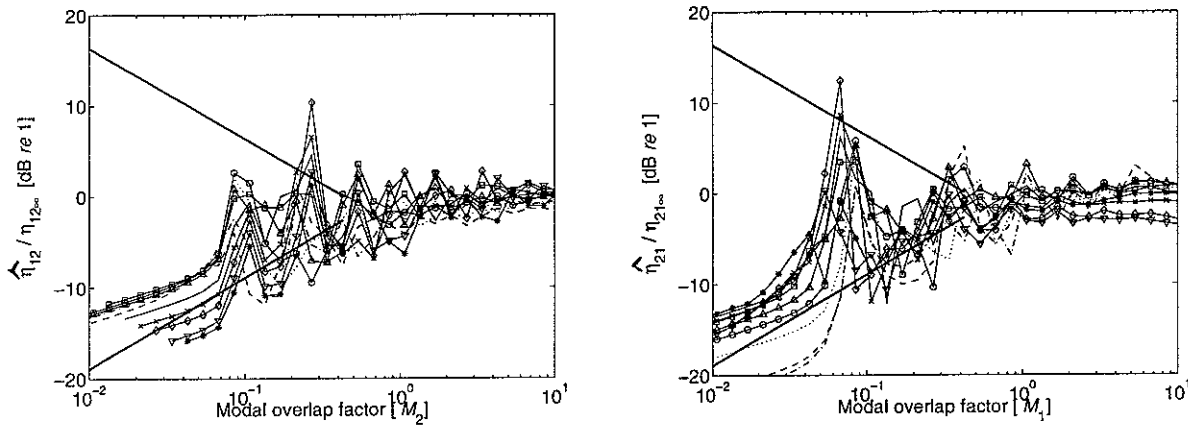

(b) the CLF ratio plotted against the modal overlap factor for the receiver plate

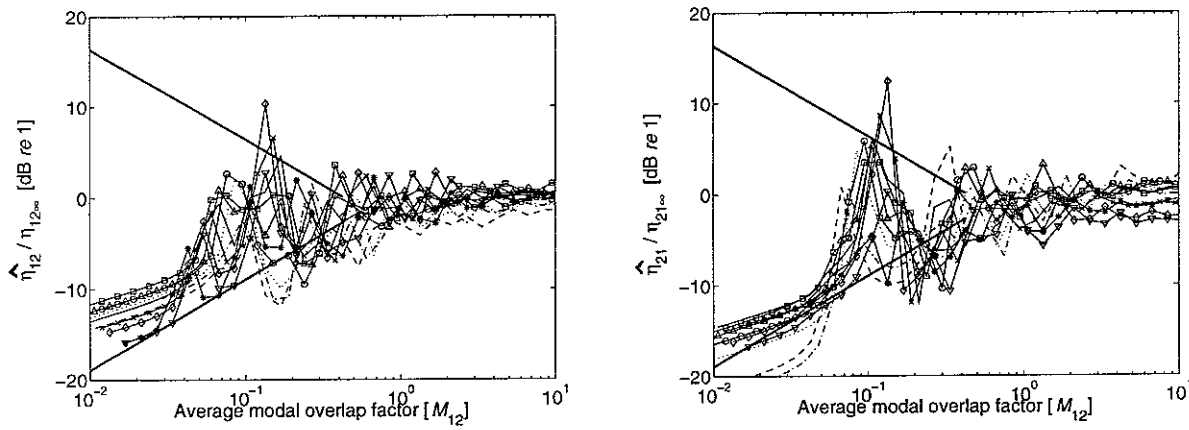

(c) the CLF ratio plotted against the geometric mean modal overlap factor [M_{12}]

Figure 5.1. CLF ratio for thickness ratio (h_1/h_2) plotted against the modal overlap factor; the thickness of plate 1 (3 mm) is fixed and the thickness of plate 2 (in millimetres) varies from 9.49 to 0.949 ($f_{\text{cut-on1}}$ = 7.34 Hz, $n_1(\omega) = 0.0085$, $f_{\text{cut-on2}} \propto h_2^{1/2}$ and $n_2(\omega) \propto h_2^{-1/2}$); ---, 9.49; -·-, 7.54; ·····, 5.99; -o-, 4.75; -Δ-, 3.78; -□-, 3.00; —, 2.38; -x-, 1.89; -◊-, 1.50; -▽-, 1.19; -*-, 0.949; —, upper and lower bounds from equations (2.29, 2.33).

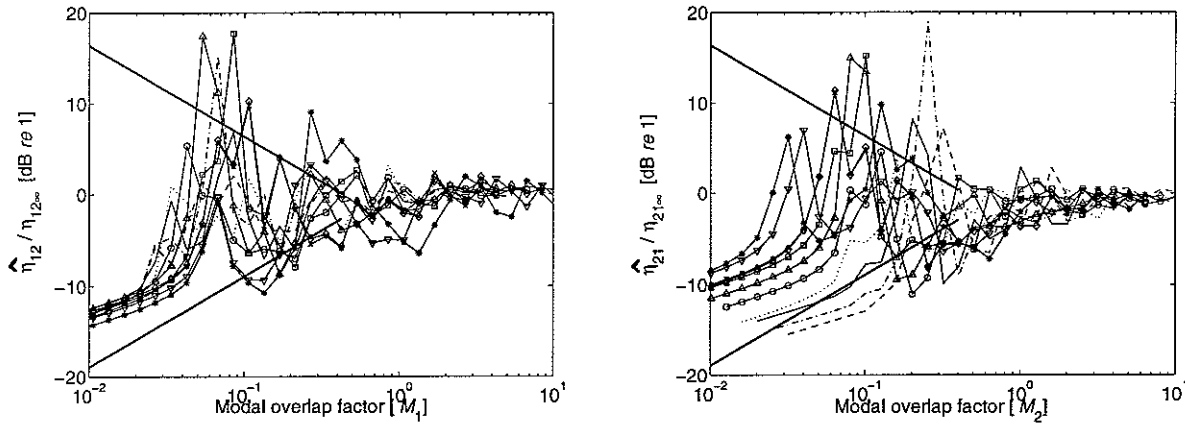

(a) the CLF ratio plotted against the modal overlap factor for the source plate

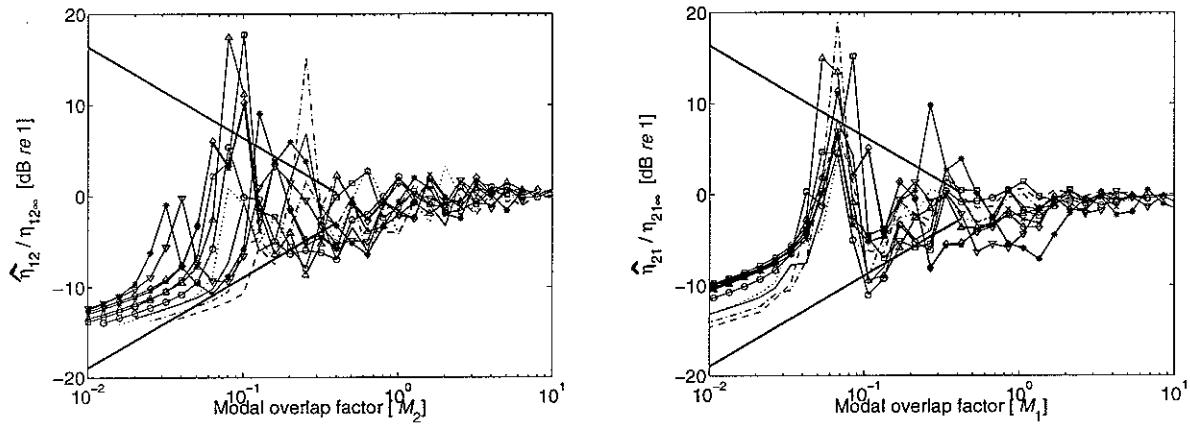

(b) the CLF ratio plotted against the modal overlap factor for the receiver plate

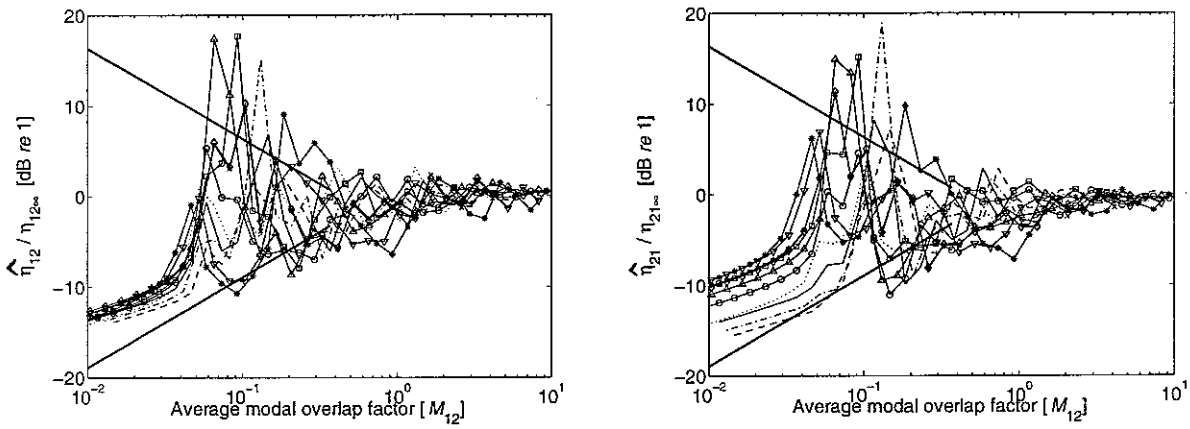

(c) the CLF ratio plotted against the geometric mean modal overlap factor [M_{12}]

Figure 5.2. CLF ratio for length ratio (L_1/L_2) plotted against the modal overlap factor; the length of plate 1 (0.5 m) is fixed and the length of plate 2 (in meters) varies from 1.58 to 0.158 ($f_{\text{cut-on1}}$ = 7.34 Hz, $n_1(\omega)$ = 0.0085, $f_{\text{cut-on2}}$ = 4.90 Hz and $n_2(\omega) \propto L_2$); ---, 1.58; -·-, 1.26; —, 1.0; ····, 0.79; -o-, 0.63; -Δ-, 0.50; -□-, 0.40; -x-, 0.32; -◊-, 0.25; -▽-,0.20; -*-, 0.16; —, upper and lower bounds from equations (2.29, 2.33).

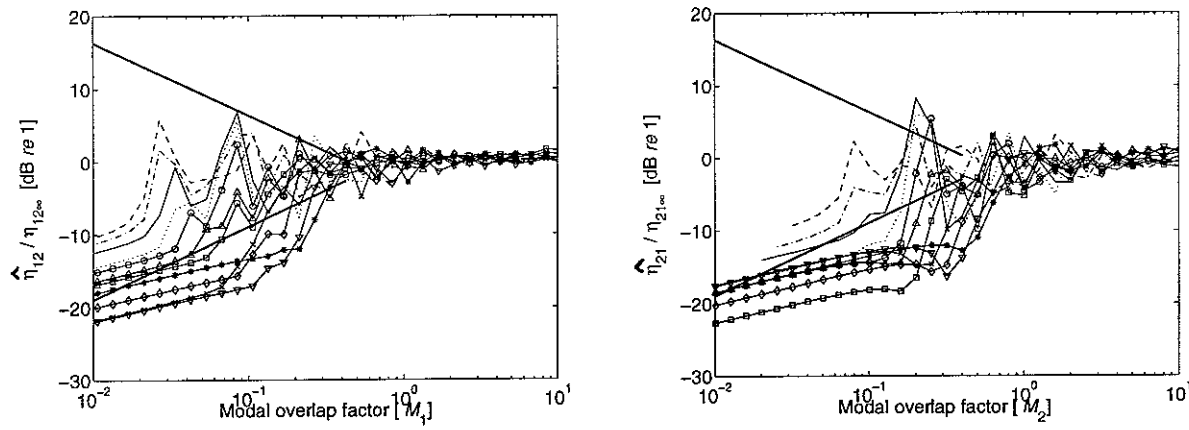

(a) the CLF ratio plotted against the modal overlap factor for the source plate

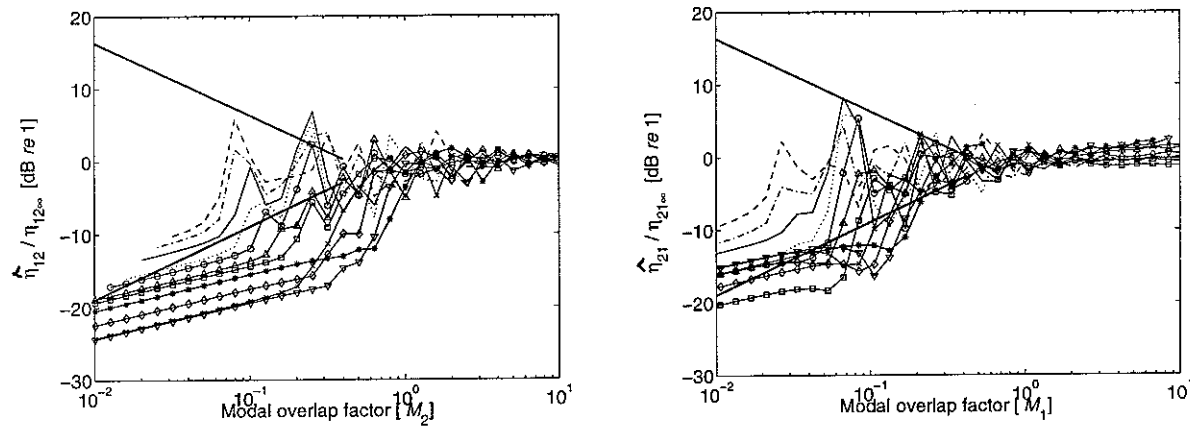

(b) the CLF ratio plotted against the modal overlap factor for the receiver plate

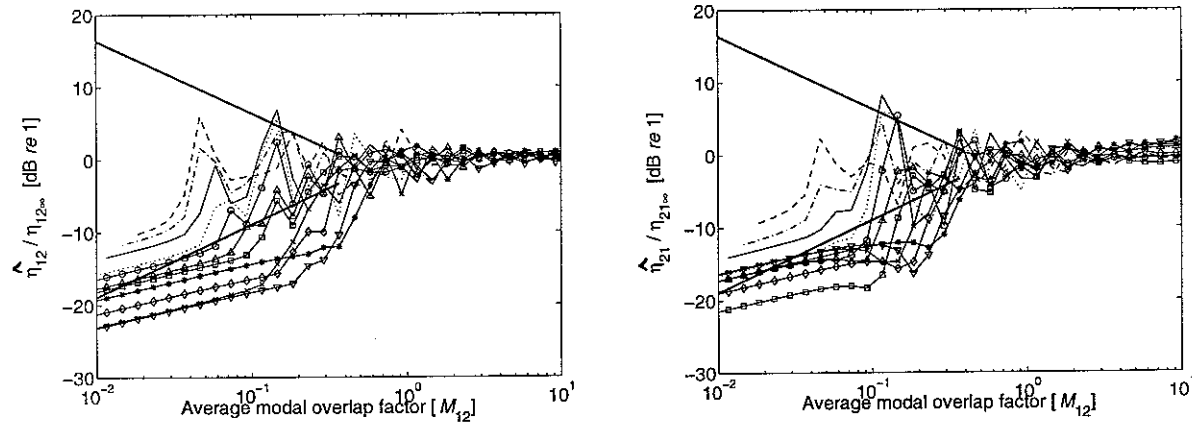

(c) the CLF ratio plotted against the geometric mean modal overlap factor [M_{12}]

Figure 5.3. CLF ratio for length/width ratio (L_1/b) plotted against the modal overlap factor; the length of plate 1 (0.5 m) is fixed and the width of the two plates (in meters) varies from 1.58 to 0.158 ($f_{\text{cut-on1}} \propto 1/b_1^2$, $n_1(\omega) \propto b$, $f_{\text{cut-on2}} \propto 1/b_2^2$ and $n_2(\omega) \propto b$); ---, 1.58; -·-, 1.26; —, 1.0; ·····, 0.79; -o-, 0.63; -Δ-, 0.50; -□-, 0.40; -x-, 0.32; -◊-, 0.25; -▽-,0.20; -*-, 0.16; —, upper and lower bounds from equations (2.29, 2.33).

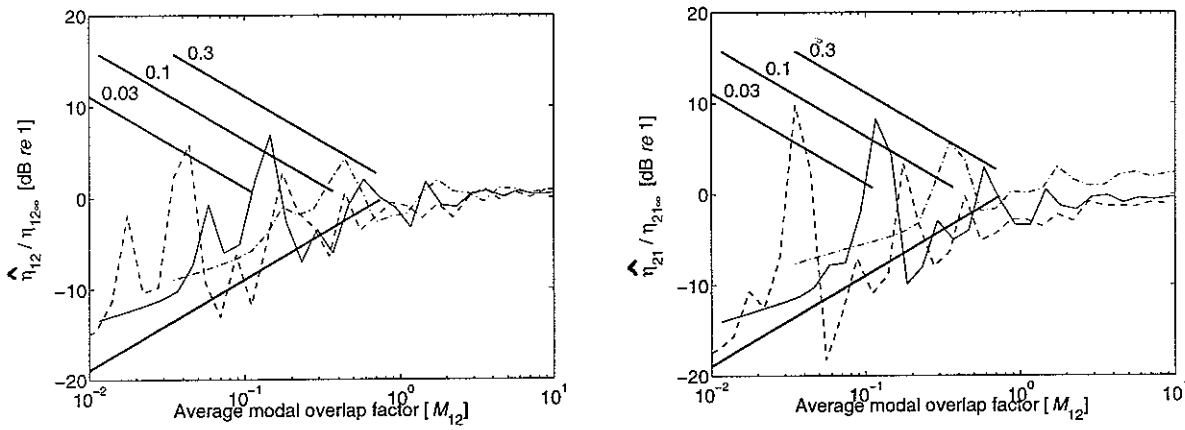

Figure 5.4. CLF ratio for different damping loss factors plotted against the geometric mean modal overlap factor; ---, $\eta = 0.03$;—, $\eta = 0.1$; ⁻·⁻, $\eta = 0.3$; —, upper and lower bounds from equations (2.29, 2.33).

Table 5.1. The average percentage of values of $\hat{\eta}_{ij}/\eta_{ij\infty}$ falling within the upper and lower bounds when plotted against the modal overlap factor for the source plate M_s, that for the receiver plate M_r and the geometric mean value $(M_sM_r)^{1/2}$.

	Parameter	M_s	M_r	$(M_sM_r)^{1/2}$
$\hat{\eta}_{12}/\eta_{12\infty}$	Thickness ratio	78	57	70
	Length ratio	76	81	77
	Length / width ratio	75	38	52
$\hat{\eta}_{21}/\eta_{21\infty}$	Thickness ratio	49	70	60
	Length ratio	65	78	74
	Length / width ratio	32	68	52

(Unit: %)

Table 5.2. The average percentage of values of $\hat{\eta}_{ij}/\eta_{ij\infty}$ falling within the upper and lower bounds ± 5dB when plotted against the modal overlap factor for the source plate M_s, that for the receiver plate M_r and the geometric mean value $(M_sM_r)^{1/2}$.

	Parameter	M_s	M_r	$(M_sM_r)^{1/2}$
$\hat{\eta}_{12}/\eta_{12\infty}$	Thickness ratio	98	98	98
	Length ratio	97	97	97
	Length / width ratio	93	71	74
$\hat{\eta}_{21}/\eta_{21\infty}$	Thickness ratio	88	97	95
	Length ratio	92	97	96
	Length / width ratio	62	95	84

(Unit: %)

6. CONCLUSIONS

In this study, some of the uncertainties in coupling loss factor estimates for a two plate system have been examined and quantified.

The effective coupling loss factor for a finite two-plate system has been directly evaluated using the Dynamic Stiffness Method. The CLF for finite plates fluctuates at low modal overlap and converges to that for semi-infinite plates at high frequencies, as expected. It has been shown that the reciprocity relationship is satisfied by the predicted CLF at high frequencies, though at low frequencies considerable variation is found.

Examination of the CLF has shown that it is related to the energy ratio and the global/local modes. The CLF estimates at low frequencies, in the region of the first few modes, contain peaks which correspond to the uncoupled modes of the receiver plate. At high frequencies, the CLF estimates for the finite plates agree with the infinite results and the transmission efficiency for the finite plates, inferred from the CLF estimates, shows good agreement with the infinite plate results. The spatial location and the number of forcing points used also affect the confidence intervals of the CLF. As the number of forcing points increases, the CLF estimates become more reliable. In order to obtain a 95% confidence interval of ± 1 dB at least 10 forcing points should be taken.

In-plane motion has also been included, although the effect is small in the examples considered. Since the cut-on frequency of in-pane motion is high, in-plane wave motion does not propagate and so does not contribute significantly to the vibrational energy at low to mid frequencies. However, if the thickness of plate is large, then in-plane motion becomes more significant.

The results of extensive parameter variations allow confidence intervals, as well as the mean CLF, to be determined at low modal overlap. For modal overlap greater than 1, the variation in CLF is small, whereas at low modal overlap most of the results fluctuate considerably. Craik's upper and lower bounds are shown to be useful estimates of the degree of variability. These can be incorporated into an SEA predictive scheme to give confidence intervals of the resulting vibration or sound pressure estimates.

REFERENCES

[1] F. J. Fahy and A. D. Mohammed 1992 *Journal of Sound and Vibration* **158**(1), 45-67. A study of uncertainty in applications of SEA to coupled beam and plate systems, Part I: Computational experiments.

[2] A. D. Mohammed 1990 *Ph.D. Thesis, University of Southampton.* A study of uncertainty in applications of Statistical Energy Analysis.

[3] B. R. Mace 1992 *Journal of Sound and Vibration* **154**(2), 289-319. Power flow between two continuous one-dimensional subsystems: a wave solution.

[4] L. Cremer, M. Heckl and E. E. Ungar 1988 *Structure-borne Sound: Structural Vibrations and Sound Radiation at Audio Frequencies.* New York: Springer-Verlag; second edition.

[5] R. H. Lyon and R. G. DeJong 1995 *Theory and Application of Statistical Energy Analysis.* Boston, Massachusetts: Butterworth-Heinemann; second edition.

[6] R. J. M. Craik 1996 *Sound transmission through buildings using Statistical Energy Analysis.* Gower Publishing Ltd.

[7] C. R. Fredo 1997 *Journal of Sound and Vibration* **199**(4), 645-666. A SEA-like approach for the derivation of energy flow coefficients with a finite element model.

[8] C. Simmons 1991 *Journal of Sound and Vibration* **144**(2), 215-227. Structure-borne sound transmission through plate junctions and estimates of SEA coupling loss factors using the finite element method.

[9] J. A. Steel and R. J. M. Craik 1994 *Journal of Sound and Vibration* **178**(4), 553-561. Statistical energy analysis of structure-borne sound transmission by finite element methods.

[10] W. S. Park, D. J. Thompson and N. S. Ferguson 1999 *ISVR Technical Memorandum* No.846. The power balance of beams and plates using the Dynamic Stiffness Method.

[11] B. R. Mace 1994 *Journal of Sound and Vibration* **178**(1), 95-112. On the statistical energy analysis hypothesis of coupling power proportionality and some implications of its failure.

[12] D. A. Bies and S. Hamid 1980 *Journal of Sound and Vibration* **70**(2), 187-204. *In Situ* determination of loss and coupling loss factors by the power injection method.

[13] R. J. M. Craik, J. A. Steel and D. I. Evans 1991 *Journal of Sound and Vibration* **144**(1), 95-107. Statistical energy analysis of structure-borne sound transmission at low frequencies.

[14] E. Skudrzyk 1980 *Journal of the Acoustical Society of America* **67**(4) 1105-1135. The mean-value method of predicting the dynamic response of complex vibrations.

[15] D. J. Thompson 2000 *Lecture Notes of ISVR MSc Sound and Vibration Studies on High Frequency Structural Vibration.* Statistical Energy Analysis - introduction.

[16] R. S. Langley 1989 *Journal of Sound and Vibration* **135**(2), 319-331. Application of the dynamic stiffness method to the free and forced vibrations of aircraft panels.

[17] G. B. Warburton 1976 *The Dynamical Behaviour of Structures.* Oxford: Pergamon Press; second edition.

[18] A. N. Bercin and R. S. Langley 1996 *Computers & Structures* **59(5)**, 869-875. Application of the Dynamic Stiffness Technique to the In-plane Vibrations of Plate Structures.

[19] E. Eichler 1964 *Journal of the Acoustical Society of America* **36**(2), 344-348. Plate-edge admittance.

[20] C. Kauffmann 1998 *Journal of the Acoustical Society of America* **103**(4), 1874-1884. Input mobilities and power flows for edge-excited, semi-infinite plates.

[21] A. N. Bercin 1996 *Journal of Sound and Vibration* **191**(5), 661-680. An assessment of the effects of in-plane vibrations on the energy flow between coupled plates.

[22] R. G. DeJong 1999 *Proceeding of IUTAM symposium on Statistical Energy Analysis*, 71-82 (F. J. Fahy and W. G. Price editors). An approach to the Statistical Energy Analysis of strongly coupled systems, Kluwer Academic Publishers.

[23] C. Boisson, J. L. Guyader, P. Millot and C. Lesueur 1982 *Journal of Sound and Vibration* **81**(1), 93-105. Energy transmission in finite coupled plates, part II: application to an L shaped structure.

[24] M. P. Norton 1989 *Fundamentals of noise and vibration analysis for engineers*, Cambridge University Press.

APPENDIX A: Expressions for the coupling loss factor between two plates joined at right angles

A.1 Introduction

The whole area of coupling loss factors is a source of confusion to would-be users of SEA. Even for the relatively simple case of two plates joined at right angles there are a number of apparently conflicting results in the literature. This appendix surveys and compares some of these results, for the case where in-plane vibration is assumed to be negligible.

A.2 Preliminaries

Consider two plates joined along a line of length L. They have thicknesses h_i, areas S_i, Young's moduli E_i, material densities ρ_i and Poisson's ratios ν_i.

The **group velocity** of bending waves in plate i,

$$c_{gi} = 2c_{Bi} = 2(\omega \kappa_i c_{Li}')^{1/2} \tag{A.1}$$

where $\kappa_i = h_i / \sqrt{12}$ is the radius of gyration and

$$c_{Li}' = \left(\frac{E_i}{\rho_i (1-\nu_i^2)} \right)^{1/2} \tag{A.2}$$

is the longitudinal wavespeed. The **wavenumber**,

$$k_i = \frac{\omega}{c_{Bi}} = \left(\frac{\omega}{\kappa_i c_{Li}'} \right)^{1/2} = \left(\frac{\omega}{h_i} \right)^{1/2} \left(\frac{12\rho_i (1-\nu_i^2)}{E_i} \right)^{1/4} \tag{A.3}$$

The asymptotic **mode count** (number of modes below frequency ω),

$$N_i(\omega) = \frac{S_i k_i^2}{4\pi} = \frac{S_i \omega \sqrt{12}}{4\pi h_i c_{Li}'} = \frac{S_i \omega}{3.6 h_i c_{Li}'} \tag{A.4}$$

(see e.g. [24], page 489)

The asymptotic **modal density** of each plate is given by $n_i(\omega) = dN_i/d\omega = dN_i/dk_i \; . \; dk_i/d\omega$

By definition, $dk_i/d\omega = 1 / c_{gi}$. Hence from equation (A.4)

$$n_i(\omega) = \frac{S_i k_i}{2\pi} \frac{1}{c_{gi}} = \frac{S_i \omega}{2\pi c_{Bi} c_{gi}} = \frac{S_i \sqrt{12}}{4\pi h_i c_{Li}'} = \frac{S_i}{3.6 h_i c_{Li}'} \tag{A.5}$$

From the definition of the **coupling loss factor**, the following reciprocity relation applies

$$n_1 \eta_{12} = n_2 \eta_{21} \tag{A.6}$$

Therefore it is necessary that

$$\frac{\eta_{12}}{\eta_{21}} = \frac{n_2}{n_1} = \frac{S_2 h_1 c_{L1}'}{S_1 h_2 c_{L2}'} \tag{A.7}$$

A.3 Coupling loss factor in terms of power transmission coefficient

Cremer and Heckl [4] (page 486) give an expression for the coupling loss factor of two two-dimensional systems joined along a line in terms of the energy transmission coefficient, τ_{12},

$$\eta_{12} = \frac{c_{g1} L \tau_{12}}{\pi \omega S_1} \tag{A.8}$$

This expression is also given by Craik [6], page 104, and Norton [24], page 407.

Equation (A.8) is derived in [4] from the fact that the mean free path length on plates is $l_m = \pi S/P$ (where P is the total length of the perimeter, see p427 of [4]) and c_{gi} is the speed of energy propagation. Hence the power (rate of flow of energy) arriving at the perimeter is

$$P_{inc,P} = \frac{E_1 c_{g1}}{l_m} \tag{A.9}$$

where E_1 is the stored energy in system 1. The power flowing to the perimeter segment L is

$$P_{inc} = \frac{E_1 c_{g1}}{l_m} \frac{L}{P} = \frac{E_1 c_{g1} L}{\pi S_1} \tag{A.10}$$

Of this, from the definition of τ_{12}, the transmitted power is the proportion $P_{12} = \tau_{12} P_{inc}$. From the definition of coupling loss factor,

$$P_{12} = \eta_{12} \omega E_1 \tag{A.11}$$

Eliminating E_1 from equations (A.10) and (A.11), equation (A.8) is obtained.

NB The power transmission coefficient τ_{12} should be derived on the assumption of diffuse incidence at the edge. In order to be consistent with equation (A.6) it is necessary for $\tau_{12} \neq \tau_{21}$. In fact

$$\frac{\tau_{12}}{\tau_{21}} = \frac{\eta_{12} c_{g2} S_1}{\eta_{21} c_{g1} S_2} = \left(\frac{h_1 c_{L1}'}{h_2 c_{L2}'} \right)^{1/2} \tag{A.12}$$

A.4 Normal incidence power transmission coefficient

Equation (A.8) contains the random incidence power transmission coefficient τ_{12}. Several of the textbooks consider first the coefficient for normal incidence, $\tau_{12}(0)$ for a line connection for a right-angled joint.

Lyon [5], page 194, gives this in the form

$$\tau_{12}(0) = \frac{4 R'_{1\infty} R'_{2\infty}}{\left| Z'_{1\infty} + Z'_{2\infty} \right|^2} \tag{A.13}$$

where $Z'_{i\infty}$ is the *line* impedance of semi-infinite system i at the connection and $R'_{i\infty}$ is the real part of $Z'_{i\infty}$. For the case of two plates joined at an angle, the appropriate impedances are the *moment* impedances (because the displacement at the connection is effectively pinned) of a semi-infinite *beam* of unit width (variations across the width of the joint are eliminated by the assumption of normal incidence). Thus, from [4] page 317

$$Z'_{i\infty} = \frac{\rho_i h_i c_{Bi}}{2 k_i^{\,2}} (1 - j) \tag{A.14}$$

Substituting from equations (A.1) and (A.3),

$$Z'_{i\infty} = \frac{\rho_i h_i^{\,5/2} c'^{\,3/2}_{Li}}{2 \omega^{-1/2} (12)^{3/4}} (1 - j) \tag{A.15}$$

Noticing that $Z'_{i\infty} = (1-j)\, R'_{i\infty}$, equation (A.13) can be rearranged as

$$\tau_{12}(0) = \frac{2}{\left(\sqrt{\frac{R'_{1\infty}}{R'_{2\infty}}} + \sqrt{\frac{R'_{2\infty}}{R'_{1\infty}}} \right)^2} \tag{A.16}$$

Writing (cf [4], p349 and [6] p108)

$$\chi = \frac{k_2}{k_1} = \left(\frac{c_{L1} h_1}{c_{L2} h_2} \right)^{1/2} \tag{A.17a}$$

$$\psi = \frac{D_2 k_2^{\,2}}{D_1 k_1^{\,2}} = \frac{\rho_2 c_{L2} h_2^{\,2}}{\rho_1 c_{L1} h_1^{\,2}} \tag{A.17b}$$

where $D_i = E_i h_i^3/12(1-\nu^2)$ is the bending stiffness, equation (A.16) can be rearranged into the form

$$\tau_{12}(0) = \frac{2}{\left(\sqrt{\frac{\psi}{\chi}} + \sqrt{\frac{\chi}{\psi}} \right)^2} \tag{A.18}$$

With slight differences in notation, this form is given by Norton [24], page 407. It is derived from first principles by Cremer and Heckl [4], page 354-356, where the additional effects of in-plane motion are also considered ('the high frequency situation'). Where the two plates are of the same material, $\psi = \sigma^2$ and $\chi = \sigma^{-1/2}$, with $\sigma = h_2/h_1$ and (see page 357 of [4])

$$\tau_{12}(0) = \frac{2}{\left(\sigma^{5/4} + \sigma^{-5/4} \right)^2} \tag{A.19}$$

The maximum value of $\tau_{12}(0)$, for two identical plates, is 0.5.

A.5 Oblique incidence power transmission coefficient

Cremer and Heckl [4], page 436-439, analyse the case of transmission for oblique incidence at a right-angled joint. Their result is

$$\tau_{12}(\theta) = \frac{2\psi \sqrt{\chi^2 - s^2} \sqrt{1 - s^2}}{\psi^2 + \psi \left(\sqrt{\chi^2 + s^2} \sqrt{1 + s^2} + \sqrt{\chi^2 - s^2} \sqrt{1 - s^2} \right) + \chi^2} \tag{A.20}$$

where $s = \sin\theta$. For $s = 0$ this reduces to equation (A.18). Importantly, $\tau_{12}(\theta) \neq \tau_{21}(\theta)$ except where $\chi = 1$. Figure A.1 shows examples (cf. Fig V/34 in [4]). For the case where $h_2 = 2h_1$ there is total reflection for angles greater than $\pi/4$ ($\sin\theta = 0.707$).

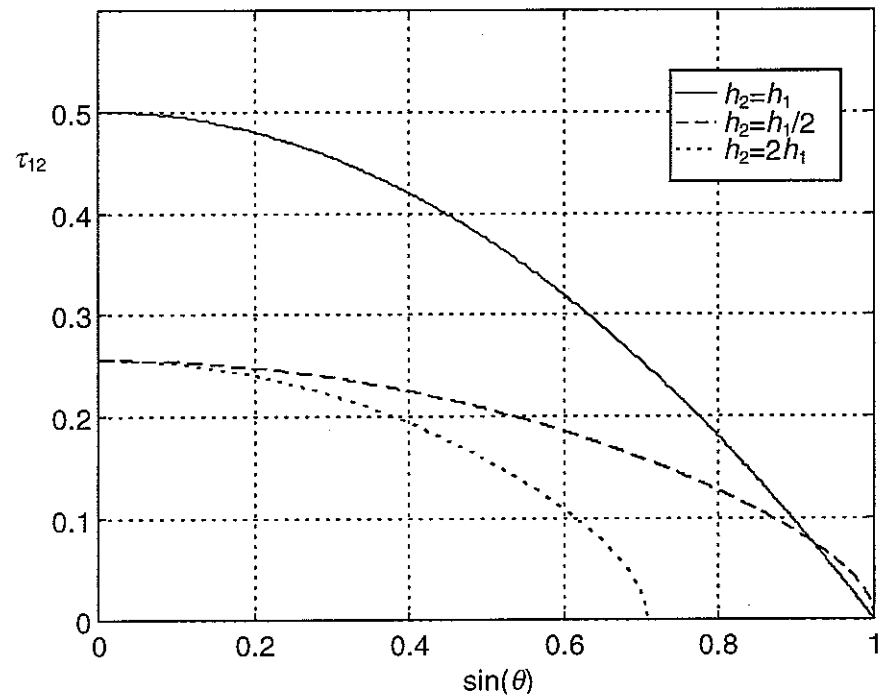

Figure A.1. Oblique angle power transmission coefficient for two plates of identical material and different thickness ratios joined at right angles (based on equation (A.20), from [4]).

To obtain a diffuse field incidence power transmission coefficient from the above, it may be assumed that energy is equally likely to propagate at all angles. Then the incident power is given by

$$P_{inc,d} = \int_0^{\pi/2} \cos\theta P_{inc}(\theta) d\theta = P_{inc}(\theta) \int_0^{\pi/2} \cos\theta d\theta = P_{inc}(\theta) \tag{A.21}$$

and the transmitted power by

$$P_{12,d} = \int_0^{\pi/2} \tau_{12}(\theta) \cos\theta P_{inc}(\theta) d\theta = P_{inc}(\theta) \int_0^{\pi/2} \tau_{12}(\theta) \cos\theta d\theta \tag{A.22}$$

Hence

$$\tau_{12,d} = \int_0^{\pi/2} \tau_{12}(\theta) \cos\theta d\theta \tag{A.23}$$

Evaluating this numerically (in Matlab), curves are found for $\tau_{12,d}$ and, by reversing h_1 and h_2, also for $\tau_{21,d}$. These results are shown in Figure A.2.

From equations (A.12) and (A.17a) it is required that $\tau_{12,d} = \chi\tau_{21,d}$. This is found to be satisfied by the results. Note that the maximum value of $\tau_{12,d}$ is 1/3, i.e. 2/3 of the maximum of $\tau_{12}(0)$. This can be obtained by direct integration of equation (A.23) after substitution of $\chi = \psi = 1$ in equation (A.20).

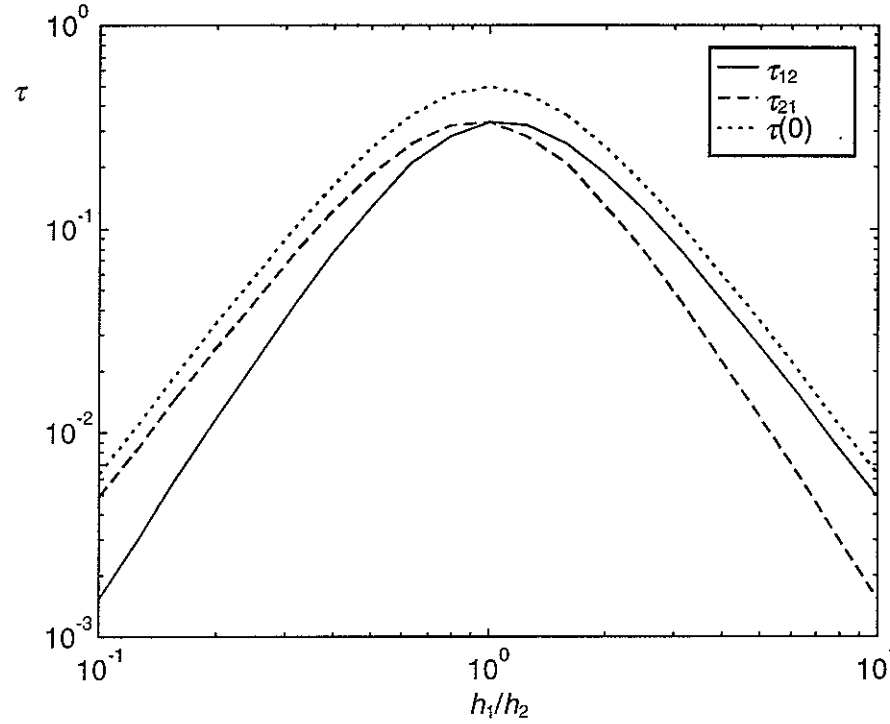

Figure A.2. Normal and diffuse incidence power transmission coefficients for two plates of identical material and different thickness ratios joined at right angles (based on numerical integration of equations (A.20) and (A.23)).

A.6 Approximations for diffuse field incidence power transmission coefficients

The above expressions have the disadvantage of requiring numerical integration. Therefore, several authors give approximate formulae for evaluating $\tau_{12,d}$. Craik [6], page 110, gives the following for the transmission loss $R_{12} = -10\log_{10}(\tau_{12})$:

$$R_{12} = 20\log_{10}\left(\sqrt{\frac{\psi}{\chi}} + \sqrt{\frac{\chi}{\psi}}\right) - 2.0053 + \frac{0.2535}{\chi} + 1.56\log_{10}\left(1 + \frac{1}{\chi^4}\right) \quad \text{for } \chi \geq 1 \qquad (24a)$$

$$R_{12} = 20\log_{10}\left(\sqrt{\frac{\psi}{\chi}} + \sqrt{\frac{\chi}{\psi}}\right) - 2.0053 + 0.2535\chi + 1.56\log_{10}\left(1 + \chi^4\right) \quad \text{for } \chi \leq 1 \qquad (24b)$$

These expressions are compared with those computed above in Figure A.3. In fact equations (A.24) produce expressions which satisfy $\tau_{12,d} = \tau_{21,d}$, which is invalid according to equation (A.6).

In Figure 4.11 of Craik [6] R_{12} is plotted. This shows a result which is *asymmetric* in h_1/h_2. This suggests a mistake in Table 4.3 of [6]. Figure A.3 also shows the result of using equation (A.24a) for all values of χ. However, this function also does not satisfy equation (A.6) and is clearly not intended. The numerical values given in Table 4.5 of [6] correspond to those of the 'exact' curve from equations (A.20) and (A.23). For $h_1/h_2>1$, equation (A.24a) gives results which are within 0.03 dB of the numerically integrated results of Figure A.2, as also claimed in [6].

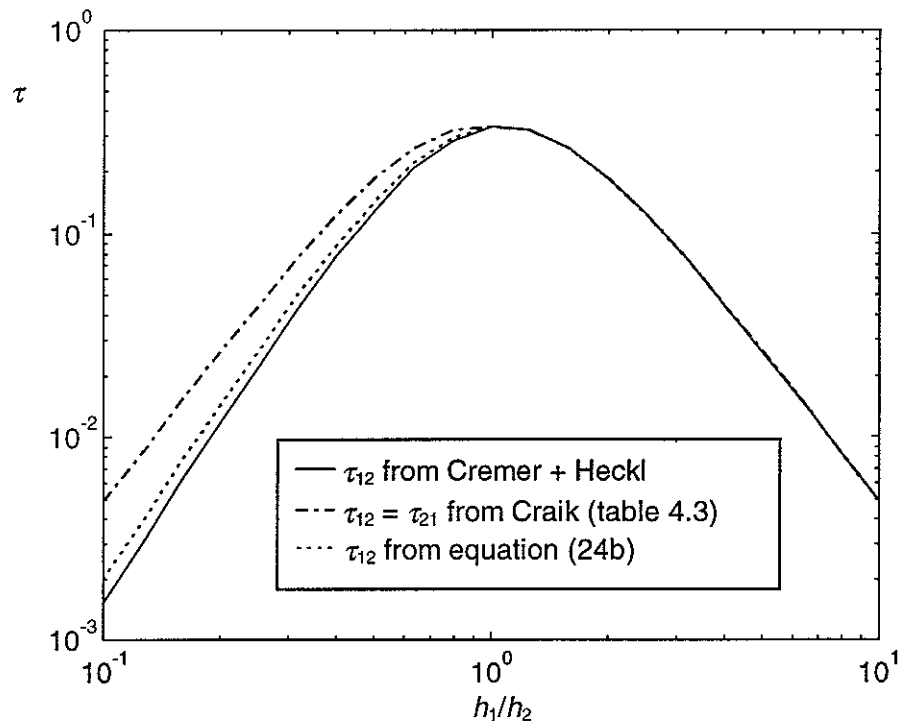

Figure A.3. Diffuse incidence power transmission coefficients for two plates of identical material and different thickness ratios joined at right angles (based on numerical integration of equations (A.20), (A.23) and on equations (A.24)).

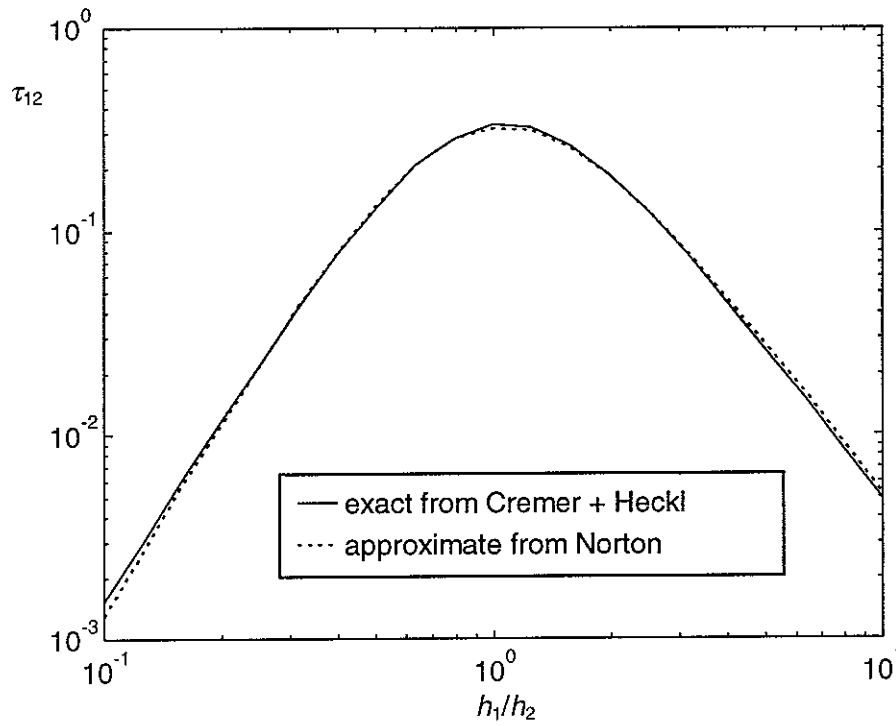

Figure A.4. Diffuse incidence power transmission coefficients for two plates of identical material and different thickness ratios joined at right angles (based on numerical integration of equations (A.20) and (A.23) and on equation (A.25)).

Norton [24] gives an alternative approximate expression, taken from Bies and Hamid [12]. This is

$$\tau_{12,d} = \tau_{12}(0)\frac{2.754\sigma}{1+3.24\sigma} \tag{A.25}$$

where $\sigma = h_1/h_2$. For $\sigma = 1$, this reduces to a factor of 0.650, close to the factor 2/3 noted above. The expression is not exactly reciprocal in σ. The ratio $n_1\eta_{12} / n_2\eta_{21}$ varies from 1 by up to a factor 1.25 (1 dB) in the range of σ shown. Figure A.4 compares results from this approximation with those from exact analysis above.

A.7 Alternative approach used by Lyon [5]

Lyon [5], pages 194-195, uses an alternative approach. He gives the following equation in terms of $\tau_{12}(0)$ rather than deriving an expression for $\tau_{12,d}$:

$$\eta_{12} = \frac{\overline{\delta f_1}}{\pi f}\beta_{corr} I_{12}(k_1, k_2)\frac{\tau_{12}(0)}{2-\tau_{12}(0)} \tag{A.26}$$

where $\overline{\delta f_1}$ is the average modal spacing, which equals $1/2\pi n(\omega)$. This means that equation (A.6) is satisfied provided that the remaining terms are symmetrical when 1 and 2 are exchanged. It has been seen earlier that this is the case for $\tau_{12}(0)$. The term β_{corr} is a correction for the damping effect of other parts of the structure and is not needed here. The term I_{12} represents an integral over angle of incidence, but it is *not* the same as equations (A.24). For the particular case of bending waves in perpendicular plates, a 'convenient curve fit' for I_{12} is given as [5]

$$I_{12} = \frac{L}{4}\left(\frac{k_1^{\,4} k_2^{\,4}}{k_1^{\,4} + k_2^{\,4}}\right)^{1/4} \tag{A.27}$$

Note that I_{12} is symmetrical in k_1/k_2. Therefore equation (A.26) satisfies the reciprocity relation equation (A.6).

In order to compare these results with the above, it is necessary to compare coupling loss factors rather than power transmission coefficients. Selecting two plates of aluminium, a frequency of 1000 Hz, and setting $h_2 = 0.003$ m, $S_1 = S_2 = 1$ m^2 and $L = 1$ m, the coupling loss factors η_{12} and η_{21} are as shown in Figure A.5.

Although the curves agree for low and high values of h_1/h_2, there is a difference around the peak of the curves. However, this can be attributed to the term $2-\tau_{12}(0)$ in the denominator of equation (A.26). Replacing this by 2 leads to agreement within less than 0.08 dB over the whole range shown.

The origin of this term, is that Lyon considers waves normally incident from a semi-infinite undamped plate. If the incident energy is E_{inc}, the transmitted energy $\tau_{12}(0)E_{inc}$ and the reflected energy $[1-\tau_{12}(0)]E_{inc}$. Thus the total energy in plate 1 is $[2-\tau_{12}(0)]E_{inc}$.

On the other hand, Cremer and Heckl's analysis is based on an underlying assumption that the field is diffuse, that is that energy is equally likely to flow in any direction. This corresponds to the case where the internal losses are greater than the coupling losses.

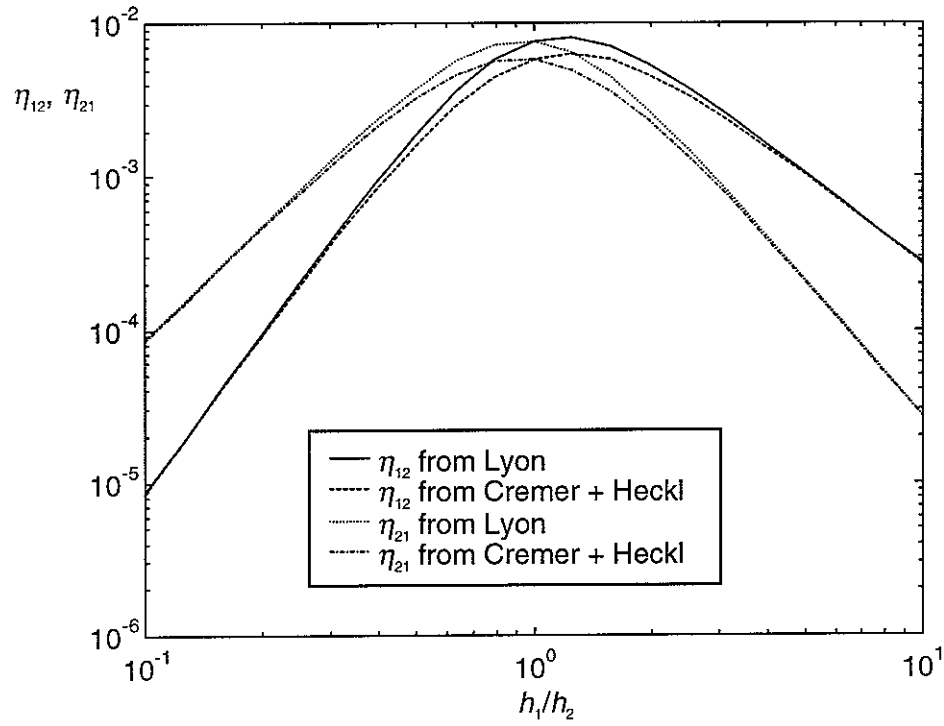

Figure A.5. Coupling loss factors for two plates of identical material and different thickness ratios joined at right angles (based on numerical integration of equation (A.20, A.23) and on equations (A.26, A.27)).

A.8 Discussion

Expressions from a number of sources for the coupling loss factors of perpendicular plates have been compared. It is shown that, although for normal incidence $\tau_{12} = \tau_{21}$, this is not the case for a general angle of incidence, nor for random incidence. It is found that most of the published results are consistent, with the exception that the expression in Table 4.3 of Craik [6] is incorrect for $\chi<1$. Apart from this, Craik's formulae give a closer approximation to the exact result (0.03 dB) than Lyon's (0.08 dB) or Norton's (1 dB) in the range considered.

The presence of the term $2-\tau_{12}(0)$ in Lyon's expression is correct for his assumptions but not for a truely diffuse field as assumed by Cremer and Heckl. However, in the latter case, the term β_{corr} in Lyon's expression is also required.